

Quantum mechanical closure of partial differential equations with symmetries

Chris Vales^{a,*}, David C. Freeman^a, Joanna Slawinska^a, Dimitrios Giannakis^a

^a*Department of Mathematics, Dartmouth College, Hanover, NH 03755, USA*

Abstract

We develop a statistical framework for the dynamical closure of spatiotemporal dynamics governed by partial differential equations. Employing the mathematical framework of quantum mechanics to embed the original classical dynamics into a quantum mechanical representation, we use the space of quantum density operators to model the unresolved degrees of freedom of the original dynamics in a statistical sense, and the framework of quantum measurement to predict their contributions to the resolved dynamics. The embedded dynamics is discretized by a positivity preserving process, leading to a compressed representation that is invariant under the dynamical symmetries of the resolved dynamics. We present a data based formulation of the closure scheme and apply it to a closure problem for the shallow water equations. The numerical results demonstrate that our closure model can accurately predict the main features of the true dynamics, including for out of sample initial conditions.

Keywords: dynamical closure, parametrization, quantum mechanics, kernel methods, delay embedding, transfer operator, shallow water equations

1. Introduction

Complex dynamical systems often encompass degrees of freedom that evolve over a wide range of temporal and spatial scales, with their evolution potentially depending on different physical regimes. A challenging problem in such multiscale, multiphysics systems is incorporating dynamical information for degrees of freedom that either are too computationally expensive to simulate directly, or depend on fully or partially unknown physical processes [1–3].

The approach employed by *closure* or *parametrization* methods is to derive surrogate dynamical models that can be used to approximate the contributions of fine grain degrees of freedom to the dynamics of coarse grain processes we can simulate consistently. Early applications included turbulent flows and climate modeling [1, 4, 5], but closure methods have since found consequential applications in a wide range of fields [6]. For example, in atmospheric dynamics a technique known as super-parametrization employs column models with explicitly resolved cloud microphysics as surrogate models of small scale moist convection, embedded within the discretization cells of a coarse atmospheric model [7, 8]. In plasma dynamics there are ongoing efforts to derive models for subgrid scale processes in fluid models, as well as to derive fluid closures of kinetic models, incorporating both physical modeling and data based approaches [9–12].

In this work we focus on the development of a statistical, data based framework for the closure of dynamics governed by partial differential equations (PDEs). More specifically, we employ the operator theoretic framework of quantum mechanics to define surrogate dynamical models, using quantum density operators to encode statistical information about fine grain degrees of freedom and quantum observables to model their contributions to the coarse dynamics. Our approach extends a previously developed quantum mechanical closure (QMCI) framework [13] to the closure of spatiotemporal dynamics, explicitly taking

*Corresponding author.

Email addresses: chris.vales@dartmouth.edu (Chris Vales), david.c.freeman.gr@dartmouth.edu (David C. Freeman), joanna.m.slawinska@dartmouth.edu (Joanna Slawinska), dimitrios.giannakis@dartmouth.edu (Dimitrios Giannakis)

into account the presence of dynamical symmetries to improve the numerical efficiency and training data requirements of our surrogate models [14].

In the rest of Section 1 we briefly discuss the problem of dynamical closure and different modeling approaches toward addressing it, present the main aspects of our proposed closure scheme and summarize the main results of this work. In Section 2 we develop in detail the different aspects of our closure framework. In Section 3 we present an application to a closure problem for the shallow water equations, followed by a brief conclusion in Section 4. Finally, Appendix A provides additional details on the numerical implementation of our closure scheme. The code used to generate the numerical results and plots of this work is available online¹.

1.1. Dynamical closure

We consider a dynamical system $\Phi^t: X \rightarrow X$, $t \geq 0$ on a state space X . The flow map Φ^t represents the spatiotemporal dynamics governed by a PDE on a bounded spatial domain S . As such, the state space X is a Hilbert space of functions on the considered spatial domain. To define the general dynamical closure problem, we decompose the state space as $X = X_r \oplus X_u$, with X_r denoting the state space of the resolved degrees of freedom of the dynamics and X_u the state space of the unresolved degrees. The flow map of the original dynamics Φ^t can then also be decomposed into the resolved dynamics $\Phi_r^t: X \rightarrow X_r$ and the unresolved dynamics $\Phi_u^t: X \rightarrow X_u$.

To provide an illustrative example of this decomposition we consider the advection equation with periodic boundary conditions

$$\partial_t u + c \partial_x u = F(u) \quad (1)$$

where u denotes a function of time $t \geq 0$ and space $x \in S \subset \mathbb{R}$, F a nonlinear function of u , and $c \in \mathbb{R}$ the advection velocity. We define the spatially averaged state function

$$\hat{u}(\cdot, x) = \frac{1}{\ell} \int_{x-\ell/2}^{x+\ell/2} u(\cdot, y) dy$$

where $\ell > 0$ denotes the length of the averaging window. The evolution equation for \hat{u} is derived by spatially averaging (1) to obtain

$$\partial_t \hat{u} + c \partial_x \hat{u} = F(\hat{u}) + G(\hat{u}, u) \quad (2)$$

with residual term

$$G(\hat{u}, u)(\cdot, x) = \frac{1}{\ell} \int_{x-\ell/2}^{x+\ell/2} F(u)(\cdot, y) dy - F(\hat{u})(\cdot, x). \quad (3)$$

A version of this type of spatial averaging on a discretized spatial domain will be used for our numerical application in Section 3.

We consider the original PDE (1) as the equation generating the true dynamics Φ^t with $u \in X$ as the state variable. Motivating the decomposition described above, we take the spatially averaged equation (2) as the equation governing the resolved dynamics, meaning that \hat{u} is the resolved state variable with state space X_r and Φ_r^t the flow map governing its evolution. The associated unresolved state space X_u is then implicitly defined as the orthogonal complement of X_r in X , representing phenomena that cannot be resolved by \hat{u} .

Due to the nonlinear term $F(u)$ in the original PDE, the spatial averaging operation has not eliminated the dependence of (2) on the unresolved degrees of freedom. This is clearly demonstrated by the presence of the residual terms (3), which retain their dependence on the original state variable u . As a result, the resolved dynamics map Φ_r generated by (2) requires at least partial knowledge of unresolved variables at any given time. This is a manifestation of the *dynamical closure problem*: to form a closed system of evolution for the resolved degrees of freedom, we need knowledge of additional, unresolved variables. The residual terms (3) still depending on the unresolved degrees of freedom are often referred to as the flux terms or *fluxes*.

¹https://github.com/cval26/qmcl_swe

To address this problem, *closure* or *parametrization methods* construct a surrogate model for the resolved degrees of freedom, which approximates the evaluation of the fluxes by modeling the unresolved variables appropriately. The surrogate models formed for the resolved and unresolved variables can then evolve in parallel, leading to a closed system of evolution for the resolved variables. To be useful, the model employed for the unresolved variables has to be computationally efficient and lead to surrogate dynamics that constitutes an effective and consistent approximation of the original dynamics in an appropriate sense.

Closure problems in physics also arise when deriving a fluid model from a kinetic description of a system by considering the evolution of moments of the phase space probability density function [15]. In that setting, the resolved variables are the low order velocity moments involved in the fluid description—usually mass, momentum and energy—while the unresolved variables are the ignored higher order moments. To define a closed system of evolution for the fluid model, one is again tasked with forming a surrogate model to estimate the required fluxes.

1.2. Modeling approaches

One approach toward defining a surrogate model is to model the unresolved variables by a deterministic function of the resolved variables. Defining such a function can be achieved by both physical modeling and data based approaches [3, 16–19]. A drawback of this approach is that it corresponds to a reduction in the dimension of the full state space of the dynamics, thereby potentially reducing the overall complexity that can be produced by the surrogate model [20].

Our work is motivated by an alternative, statistical approach, where the state space of the unresolved degrees of freedom is replaced by the space of probability density functions on the full state space of the dynamics [21–23]. More specifically, a probability density function is used to assign a probability that the dynamical system is in a given state at a given time. Contrary to purely functional approaches, where a single state of the system is uniquely identified for any given time, statistical methods take into consideration the presence of uncertainty in our knowledge of the full state of the dynamical system.

To illustrate the main features of this approach we define a probability density function $p \in L^1(X)$ on the state space. This is a real valued, nonnegative function whose integral over X is equal to one with respect to an appropriate measure. At any given time, the evaluation of the density function $p(u) \geq 0$ assigns a probability that the dynamical system is currently in state $u \in X$. Equipped with statistical knowledge of the current state of the dynamics, one can use it to compute the fluxes required for the evolution of the resolved variables. To that end, the fluxes are modeled by a bounded, real valued function $f \in L^\infty(X)$ called an observable; namely, given a state $u \in X$, the associated flux is $f(u) \in \mathbb{R}$. The required flux can then be estimated by the expected value of f with respect to p , namely $\int_X f(u)p(u)du \in \mathbb{R}$ with respect to an appropriate measure.

Having estimated the required flux term, one can then proceed with the evolution of the resolved variables; in our motivating example, this corresponds to integrating in time the spatially averaged PDE. For the surrogate evolution system to be closed, it must also account for the time evolution of the surrogate model of the unresolved variables, namely the density function p . This can be accomplished by using the transfer or Perron-Frobenius operator, which governs the evolution of probability density functions under the dynamics [24]. These notions will be made precise in the following sections.

As explained in the following section, one of the main features differentiating our closure framework from the general statistical framework sketched above is that we replace the probability density function p with a probability density operator. Namely, the nonnegative function p with unit integral is replaced by a positive semidefinite operator with unit trace. Accordingly, the bounded function f modeling the fluxes is replaced by a bounded operator. In our framework, the estimated flux is then given by the expected value of the observable operator with respect to the probability density operator.

1.3. Quantum mechanical closure framework

We provide a brief overview of the QMCI framework as it has been developed in [13] for the closure of dynamics governed by ordinary differential equations. A detailed treatment of the framework will be given in Section 2, where we extend it to the closure of dynamics governed by PDEs.

As already mentioned earlier, we adopt a statistical description of the unresolved dynamics, meaning that we model the evolution of a probability density function of the state vectors, rather than the evolution of the state vectors themselves. One of the main features of the QMCI framework is that this statistical description is embedded into the operator setting of quantum mechanics on a complex Hilbert space $H = L^2(X, \mu)$, where X denotes the state space and μ an invariant probability measure of the original dynamics. This involves embedding observables and probability densities, as well as the evolution of said densities under the dynamics and their bayesian conditioning.

In the classical statistical description, a probability density function $p \in L^1(X, \mu)$ was used to model the state of the unresolved degrees of freedom. Given that $\sqrt{p} \in H$, we now map function p to the quantum density operator $\rho \in B(H)$, $\rho = \langle \sqrt{p}, \cdot \rangle \sqrt{p}$, representing a pure quantum state. Quantum density operators—also called quantum states—are positive semidefinite, selfadjoint operators in $B(H)$ with unit trace, and can be thought of as the operator analog of probability density functions. In this work we mainly use pure quantum states, which are rank-one quantum density operators equivalent to projections along a unit vector [25, 26]. The statistical description of the dynamics obtained by mapping the density function p to the density operator ρ is an example of the Koopman-von Neumann representation of classical dynamics [27–29].

The fluxes needed for the closure of the resolved dynamics were modeled classically by an observable $f \in L^\infty(X, \mu) \subset H$. This is now mapped to a selfadjoint multiplication operator $A \in B(H)$, $Ag = fg$ for all $g \in H$, which is referred to as a quantum observable. With these definitions in place, the surrogate flux needed for the evolution of the resolved dynamics is defined as the expected value of A with respect to ρ , namely $\mathbb{E}_\rho A = \text{tr}(\rho A) \in \mathbb{R}$, which is connected to the theory of quantum measurement. In other words, we use the space of quantum density operators to model the unresolved degrees of freedom of the dynamics and the framework of quantum measurement to estimate their fluxes.

In addition to evaluating the required flux terms, we need to be able to evolve the density operator ρ under the system’s dynamics and condition it based on observed dynamical behavior. In the classical case, the square root of the probability density function \sqrt{p} evolved according to the transfer or Perron-Frobenius operator $P: H \rightarrow H$, $P\sqrt{p} = \sqrt{p} \circ \Phi^{-1}$. Accordingly, the evolution of the density operator ρ is governed by the induced transfer operator $\mathcal{P}: B(H) \rightarrow B(H)$, acting by conjugation $\mathcal{P}\rho = P\rho P^{-1}$.

In analogy to the bayesian conditioning of the probability density function p , we can condition the density operator ρ using a quantum effect operator $e \in B(H)$

$$\rho|_e = \frac{\sqrt{e}\rho\sqrt{e}}{\mathbb{E}_\rho e} \quad (4)$$

where \sqrt{e} denotes the positive square root of e . The above equation can be interpreted as the operator analog of the classical Bayes rule [30]. In addition, the quantum effect operator e can be thought of as the operator analog of an indicator function, which is used in classical probability to represent an event, namely a set in the event space. For instance, for a given set $F \subset X$ we can build the indicator function $1_F \in H$ taking the value one on F and zero elsewhere. The quantum effect operator $e_F \in B(H)$ can then be defined as multiplication by 1_F , namely $e_F g = 1_F g$ for all $g \in H$.

The following diagram depicts the evolution for one timestep of the QMCI closure model built using the tools developed in the previous paragraphs. The top row of the diagram is concerned with the resolved degrees of freedom $\hat{u} \in X_r$, while the bottom row with the density operator ρ acting as our surrogate model for the unresolved degrees of freedom. In the diagram, subscripts are used to denote the time index, while Id denotes the identity map.

$$\begin{array}{ccccc}
 \hat{u}_n & \xrightarrow{\text{resolved}} & \hat{u}_{n+1} & \xrightarrow{\text{Id}} & \hat{u}_{n+1} \\
 & \nearrow \text{flux} & & \searrow \text{effect} & \\
 \rho_n & \xrightarrow{\text{transfer}} & \rho'_{n+1} & \xrightarrow{\text{Bayes}} & \rho_{n+1}
 \end{array} \quad (5)$$

To evolve the resolved variables for one timestep, we require knowledge of the flux term depending on the unresolved degrees of freedom. As explained above, this is estimated by the expected value of an observable

A with respect to the density ρ_n . The evolution of the density operator ρ_n consists of two steps, a prediction step and a correction step. The prediction step employs the transfer operator to update the density operator ρ_n , yielding the prior density ρ'_{n+1} . The correction step relies on the quantum Bayes formula (4) to correct this prediction, yielding the posterior density ρ_{n+1} . The bayesian correction uses information extracted from the updated resolved variables \hat{u}_{n+1} , in the form of a quantum effect, to condition the prior density, concluding one timestep of the evolution of the density operator.

1.4. Main results

We offer a preliminary description of the way QMCI is extended to the closure of dynamics governed by PDEs. As explained in Section 1.1, in the setting of spatiotemporal dynamics the resolved state \hat{u} is a spatially averaged function on the spatial domain S . Motivated by this, the main point of departure of the extended QMCI framework from the one outlined above is that we use a field of density operators $\rho(x)$ to model the unresolved degrees of freedom at each point x , instead of using one density operator for the whole domain. This enables us to compute surrogate fluxes that vary over the spatial domain, and are thus capable of modeling the true flux terms (3) introduced earlier. Schematically, this means that the extended QMCI scheme involves one copy of diagram (5) for each gridpoint x , with the diagrams evolving in parallel.

The main features of the present work can be summarized as follows.

1. *Positivity preservation.* Using probability density operators to encode statistical information about the original dynamics leads to a closure scheme that is positivity preserving, which is important for sign definite quantities. More specifically, positive flux terms in the original dynamics are represented by positive definite operators, in turn leading to positive surrogate flux terms in our scheme's implementation (Section 2.5).
2. *Symmetry factorization.* We incorporate elements of the vector valued spectral analysis (VSA) framework [14] to develop a data based formulation of our scheme that is efficient and effective in the presence of dynamical symmetries. More specifically, our scheme rests on a compressed approximate representation of the original dynamics that is invariant with respect to the dynamical symmetries of the resolved dynamics (Section 2.4).
3. *Computational efficiency.* The numerical implementation of our closure scheme requires solving an eigenvalue problem for a kernel matrix, which is one of the most expensive tasks of the scheme (Section 2.5). To address that we compute a low rank approximation of the original kernel matrix and use it to solve the eigenvalue problem with reduced cost [31].
4. *Application.* We apply our scheme to a closure problem for the shallow water equations on a one dimensional spatial domain (Section 3). The results demonstrate that the derived surrogate model can effectively capture and reproduce the main features of the dynamics, including for out of sample initial conditions. The numerical results can be reproduced using the provided code².

We end this section by offering a partial answer to the question: why formulate a statistical closure framework using the operator setting of quantum mechanics, instead of the original function setting of classical mechanics? First, working in an operator setting leads to an implementation of our closure scheme that is naturally positivity preserving, meaning that the required discretization of classical observables and probability density functions preserves their positivity (Section 2.5). Second, the use of density operators to encode statistical information about the unresolved degrees of freedom offers a potential increase in the available encoding capacity, compared to using density functions (Section 3.4). However, these benefits are accompanied by an increase in computation and memory cost, since most discretized quantities are now represented by matrices instead of vectors (Section 2.5). Finally, the fact that our closure scheme rests on the mathematical framework of quantum mechanics offers the opportunity to explore its future implementation in quantum computers, especially in order to investigate whether a more efficient implementation can be devised by doing so.

²https://github.com/cval26/qmcl_swe

2. Closure of partial differential equations

In this section we develop the extended QMCI closure scheme and its data based formulation. We begin by setting up the problem in Section 2.1, before presenting the main aspects of our closure modeling framework in Section 2.2. As explained in Section 2.2, the extended QMCI scheme is formulated in an infinite dimensional Hilbert space H . In Section 2.3 we construct a finite dimensional subspace of H , which will be used in the numerical implementation of our scheme. Section 2.4 then investigates some of the properties of the constructed subspace with respect to dynamical symmetries. Finally, Sections 2.5 and 2.6 deal with the data based formulation of the extended QMCI scheme that will be used for our numerical experiments.

2.1. Problem setting

Expanding on the preliminary material presented in Section 1.1, we consider the spatiotemporal dynamics $\Phi^n: X \rightarrow X$, $n \in \mathbb{N}$, possessing an invariant probability measure μ . The discrete time map Φ^n is assumed to be a discrete time version of the continuous time dynamics, with $\Phi^n = \Phi^{n\Delta t}$ for a timestep $\Delta t > 0$. Based on the guiding example of the advection equation given in Section 1.1, the dynamics map Φ^n is generated by the temporally discretized version of (2), corresponding to the spatially averaged dynamics.

The state space X of the dynamics is a Hilbert space of functions on a bounded spatial domain $S \subset \mathbb{R}^c$, $c \in \mathbb{N}$. Specifically, we assume $X \subset L^2(S, \nu; \mathbb{R}^d)$, $d \in \mathbb{N}$, with ν denoting the Lebesgue measure. We consider the state space decomposition $X = X_r \oplus X_u$ into the resolved and unresolved state spaces. Based on (1)–(2), the resolved state space is associated with spatially averaged or coarsened functions, which were denoted by \hat{u} in Section 1.1. Analogously, the unresolved state space $X_u = X_r^\perp$ is defined as the orthogonal complement, representing degrees of freedom that cannot be resolved by the coarse state \hat{u} .

Introducing the product state space $\Omega = X \times S$ and product measure $\sigma = \mu \times \nu$, we define the Hilbert space of spatiotemporal observables $H = L^2(\Omega, \sigma; \mathbb{C})$. Given a real valued observable $f \in H$, for almost every $u \in X$ we have that $f(u, \cdot) \in L^2(S, \nu; \mathbb{R})$ yields a real valued function on the spatial domain S , with $f(u, x) \in \mathbb{R}$ its value at $x \in S$. The motivation for our choice of space H is our interest in spatiotemporal observables; that is, patterns of evolution that have both a temporal dependence through $u \in X$ and a spatial dependence through $x \in S$. An example of such an observable is the flux function introduced in (3); given a state $u \in X$ and gridpoint $x \in S$, it outputs the residual term required for the local closure of the coarse dynamics (2). Moving forward, the range space of a function space is assumed to be \mathbb{C} unless explicitly noted otherwise, and the measure notation is dropped when clear from the context; for example, we write $L^2(X)$ instead of $L^2(X, \mu; \mathbb{C})$.

The fact that we employ an invariant measure μ means that the dynamics Φ^n is volume preserving—also called incompressible—when the state space “volume” is measured with μ . This means that $\mu(\Phi^{-n}(F)) = \mu(F)$ for every measurable set $F \subseteq X$ and $n \in \mathbb{N}$. For instance, there are dissipative nonlinear PDEs which, although not volume preserving with respect to the ambient Lebesgue measure, can be shown to possess an invariant measure related to their dynamics on an attractor [32, 33]. The existence of an invariant probability measure for compact X and continuous Φ^n is ensured by the Krylov-Bogoliubov theorem [24], which is sufficient for the applications considered in the present work.

In the data based formulation of our scheme treated in Sections 2.5, 2.6 and 3, we use dynamical trajectories to collect state space samples as our training data. The process of sampling the dynamics along a trajectory can be naturally interpreted as sampling an invariant measure μ , since it is the dynamics that dictates the statistical distribution of the sampled points in the state space. This may be contrasted to sampling the dynamics on a predefined cartesian grid in the state space, which would correspond to sampling the ambient Lebesgue measure.

2.2. Closure model

The flux terms needed for the closure of the resolved dynamics are represented by d classical real valued observables $f_j \in L^\infty(\Omega) \subset H$, $j \in \{0, \dots, d-1\}$. Following the approach outlined in Section 1.3, each observable f_j is mapped to a bounded, selfadjoint multiplication operator $A_j \in B(H)$, which we refer to as a quantum observable.

As mentioned earlier, an example of such an observable is the flux function (3), which generates the residual terms needed for the integration of the coarse dynamics (2). Given that the advection equation (1) models the evolution of the scalar field u , it follows that $d = 1$ and thus only one observable is needed to model the fluxes. In Section 3 we are going to consider a closure problem for the shallow water equations (14), a system of PDEs for two scalar fields (height and momentum). As a result, in that case $d = 2$ and thus two observables will be used to generate the needed fluxes.

To model the unresolved degrees of freedom we employ a field of quantum density operators $\rho: S \rightarrow B(H)$ over the discretized spatial domain S . Each density operator $\rho(x) \in B(H)$ represents the unresolved degrees of freedom of the dynamics at a point $x \in S$ in a statistical sense. It is defined as the rank-one projection along the square root of a probability density function $p_x \in L^1(\Omega)$, $\rho(x) = \langle \sqrt{p_x}, \cdot \rangle \sqrt{p_x}$. Using a field of density operators allows us to compute fluxes that vary over the spatial domain S for each quantum observable A_j . More specifically, we define the corresponding d surrogate flux functions $\tilde{f}_j: S \rightarrow \mathbb{R}$ with action

$$\tilde{f}_j(x) = \text{tr}(\rho(x)A_j) \in \mathbb{R} \quad (6)$$

yielding d surrogate flux terms at each gridpoint.

For the closure of the coarse advection dynamics (2), one density operator $\rho(x)$ is required for each gridpoint x of the spatial domain. Using equation (6) with the single quantum observable modeling the flux terms (3), we can generate one surrogate flux at each gridpoint x for each timestep, thus creating a surrogate evolution equation for the coarse dynamics.

The time evolution of each density operator $\rho(x)$ is performed by conjugation with the transfer operator $P: H \rightarrow H$, $P\sqrt{p_x}(u, \cdot) = \sqrt{p_x}(\Phi^{-1}(u), \cdot)$, yielding $\rho^{n+1}(x) = P\rho^n(x)P^{-1}$, where superscripts denote the time index. Finally, the bayesian conditioning of each density operator $\rho(x)$ is performed using a quantum effect operator $e_x \in B(H)$ and the quantum Bayes rule (4) introduced in Section 1.3. The way the quantum effects $e_x \in B(H)$ are computed in practice will be explained in Section 2.5.

2.3. Finite dimensional projection

As explained above, our extended closure model is formed in the infinite dimensional Hilbert space of observables H . In this section we form a finite dimensional subspace $H^L \subset H$ by constructing a collection of orthonormal basis functions that span H^L .

To construct a finite dimensional subspace of H we use the orthonormal basis generated by the eigenfunctions of a positive definite, selfadjoint kernel integral operator $K: H \rightarrow H$

$$Kf = \int_{\Omega} \kappa(\cdot, \omega)f(\omega)d\sigma(\omega) \quad (7)$$

with a positive definite, symmetric and uniformly continuous kernel function $\kappa \in C_b(\Omega \times \Omega) \cap L^2(\Omega \times \Omega)$. By forming an operator acting directly on the product Hilbert space H we obtain eigenfunctions that are generally not of separable, tensor product form. This is in contrast to traditional approaches such as the proper orthogonal decomposition, where one would build a basis for $L^2(X)$ (the temporal space in this context) and form its tensor product with a basis for the spatial space $L^2(S)$ to form a basis for $H \simeq L^2(X) \otimes L^2(S)$. As explained below, in the presence of dynamical symmetries our approach leads to a more compressed finite dimensional representation of the dynamics on H , meaning that each eigenfunction of operator K as defined above can represent spatiotemporal patterns that are not expressible as a product of a single pair of temporal and spatial modes [14].

The kernel function $\kappa(\omega, \omega') = k(W_Q(\omega), W_Q(\omega'))$ is formed by composing a gaussian kernel function $k: \mathbb{R}^{dQ} \times \mathbb{R}^{dQ} \rightarrow \mathbb{R}$ and a time delay embedding map $W_Q: \Omega \rightarrow \mathbb{R}^{dQ}$, where $Q \in \mathbb{N}$ denotes the number of time delays. More specifically, the map W_Q acts by

$$W_Q((u, x)) = (\text{proj}_r(u)(x), \text{proj}_r(\Phi^{-1}(u))(x), \dots, \text{proj}_r(\Phi^{-(Q-1)}(u))(x)) \quad (8)$$

which corresponds to pointwise time delay embedding of the product state sample $\omega = (u, x)$. Note that W_Q considers only the resolved component of state vector $u \in X$ by using the projection operator $\text{proj}_r: X \rightarrow X_r$.

This is because in many practical situations one has access to data only for the resolved variables, not the full state of the system. The gaussian kernel then acts by

$$k(W_Q(\omega), W_Q(\omega')) = \exp\left(-\frac{1}{\epsilon_Q} \|W_Q(\omega) - W_Q(\omega')\|^2\right) \quad (9)$$

where $\|\cdot\|$ denotes the euclidean norm in \mathbb{R}^{d_Q} and $\epsilon > 0$ is a tunable bandwidth parameter. The bandwidth parameter ϵ can be calibrated using the procedure developed in [34]. In our numerical experiments we normalize the above kernel to turn it into a bistochastic kernel. The bistochastic kernel normalization process and motivation for using it can be found in [35, 36].

The eigenfunctions of operator K from (7) form an orthonormal basis for its range $\text{ran } K \subset H$. We use its $L \in \mathbb{N}$ leading eigenfunctions $\{\phi_\ell\}_{\ell=0}^{L-1}$ to define the finite dimensional subspace $H^L \subset H$ as their linear span. Next, the density operators and observables introduced in Section 2.2 are projected from $B(H)$ to $B(H^L)$, which can be represented by $L \times L$ matrices with respect to our basis. This process will be presented in Section 2.5 along with the data based formulation of our closure scheme.

In the next section we describe some of the properties of the subspace $\text{ran } K \subset H$ obtained through the eigendecomposition of K as they relate to dynamical symmetries.

2.4. Dynamical symmetries

We build the finite dimensional subspace H^L via the eigenfunctions of the kernel integral operator K , using a kernel function that acts by time delay embedding each state vector u at a fixed gridpoint x . This choice of kernel function is motivated by the VSA framework developed in [14], where the following material is presented in more detail.

We are particularly interested in PDEs with dynamical symmetries, which often arise from symmetries on the spatial domain such as spatial translations or rotations. We stress that our closure framework does not require the presence of dynamical symmetries. However, when symmetries are present, then our choice of kernel function exhibits some favorable properties.

We consider a symmetry group G acting on the spatial domain S by a continuous left action Γ_g , which preserves the measure ν for all $g \in G$. In particular, G is the group of dynamical symmetries associated with the resolved dynamics Φ_r^n , and is generally a subgroup of the group of symmetries associated with the true dynamics Φ^n . This is because some of the original symmetries may be lost when deriving the resolved dynamics by spatial averaging or coarsening.

The actions Γ_g induce the associated actions $\Gamma_{X,g}(u) = u \circ \Gamma_g^{-1}$ on the state space X . Assuming that X_r is invariant under Γ_g , they also induce the corresponding actions $\Gamma_{r,g}(\hat{u}) = \hat{u} \circ \Gamma_g^{-1}$ on the resolved state space X_r . The induced actions represent dynamical symmetries of the resolved dynamics Φ_r^n , which means that they satisfy the equivariance property

$$\Phi_r^n \circ \Gamma_{X,g} = \Gamma_{r,g} \circ \Phi_r^n \quad (10)$$

for all $n \in \mathbb{N}$ and $g \in G$. In addition, we assume that the resolved dynamics is derived in such a way that the true flux functions $f_j \in H$ satisfy the analogous equivariance property $f_j(\Gamma_{X,g}(u), x) = f_j(u, \Gamma_g(x))$ for all $x \in S$, $u \in X$, $g \in G$ and $j \in \{0, \dots, d-1\}$. As explained below, our choice of kernel naturally exploits the equivariance property (10) to bestow an analogous invariance property on the eigenfunctions of the kernel integral operator.

As an example, the dynamics generated by the advection equation (1) with periodic boundary conditions is equivariant under the continuous group of spatial translations. The translation symmetry is preserved during the spatial averaging employed to derive the averaged equation (2). As a result, in this case both the true and the resolved (averaged) dynamics satisfy the same group of dynamical symmetries. Furthermore, in Section 3 we will consider the shallow water equations (14) with periodic boundary conditions, which are also equivariant under spatial translations. More specifically, we will consider the discretized equations on a fine grid as the true dynamics, and an averaged version on a coarse grid as the resolved dynamics. In that case, the true dynamics will be equivariant under the discrete group of translations associated with the fine

grid. However, the symmetries of the resolved dynamics will be a subgroup of that group, containing only the spatial translations on the coarser grid.

Under the action of map W_Q from (8), the product space Ω is factored into a space of equivalence classes $[\omega]_Q \subset \Omega$, $\omega \in \Omega$, with each class defined as the subset of Ω on which W_Q is constant. Namely, a product state ω' is a member of $[\omega]_Q$ if and only if $W_Q(\omega) = W_Q(\omega')$. For our choice of map W_Q , each equivalence class consists of the points in Ω whose resolved dynamical evolution over Q delays is identical. From the equivariance property (10) it follows that, for any $\omega \in \Omega$, the set of all symmetry transformations of ω under G is a subset of its equivalence class $[\omega]_Q$. This is because any product state vectors that differ only by a symmetry transformation will demonstrate the same evolution under the resolved dynamics Φ_r^n , by virtue of (10).

Because the kernel function κ in (7) acts by composition with the delay embedding map W_Q , it follows that κ is constant on the $[\cdot]_Q$ equivalence classes by construction. As a result, every function $f \in \text{ran } K$ is constant on the equivalence classes; namely, $f(\omega') = f(\omega)$ for all $\omega' \in [\omega]_Q$. Since each equivalence class $[\omega]_Q$ contains all symmetry transformations of ω under G , it follows that functions $f \in \text{ran } K$ satisfy the invariance property

$$f \circ \Gamma_{\Omega, g} = f \quad (11)$$

for all $g \in G$, with $\Gamma_{\Omega, g} = \Gamma_{X, g} \otimes \Gamma_g$ the induced group action on Ω . In particular, this implies that the eigenfunctions of the integral operator K satisfy this property as well. Combined with the fact that all $f \in \text{ran } K$ are continuous by the uniform continuity of κ , we conclude that $\text{ran } K$ consists entirely of continuous functions that are constant on the equivalence classes $[\cdot]_Q$.

As a result of (11), by using the eigenfunctions of K we derive a basis of $\text{ran } K$ that is invariant under the actions of G , instead of getting multiple ‘‘copies’’ of the same underlying functions generated by the action of different $g \in G$. Most importantly for our purposes, this means that fewer eigenfunctions are needed to represent complex spatiotemporal dynamics, thereby producing a more efficient compression of the dynamics from H to subspace H^L .

2.5. Data based formulation

In this section we consider the data based formulation of the extended QMCI scheme developed in the previous sections, using a single dynamical trajectory to generate our training data. In the next section we extend this construction to the case of training data consisting of multiple trajectories.

In the theoretical formulation of QMCI developed above, the state space X is generally an infinite dimensional Hilbert space of functions on the spatial domain S , with the dynamics map Φ^n generated by a PDE. To be able to simulate the ‘‘true’’ dynamics numerically, we approximate the true dynamics by a discretization of the original PDE associated with a discretized spatial domain $S_M \subset S$, where $M \in \mathbb{N}$ denotes the number of gridpoints. In what follows, we denote by ν_M a restriction of the Lebesgue measure ν to a σ -algebra of sets generated by the discretization cells of the spatial domain S_M .

With respect to our motivating example of the advection PDE (1), the above corresponds to considering the true discrete time dynamics Φ^n as being generated by a high fidelity discretized version of (1). The resolved dynamics and associated resolved state space are again defined by forming a spatially averaged version of the discretized true dynamics. A detailed description of this construction will be presented in Section 3, where we consider an application of QMCI to the shallow water equations.

We consider a finite dynamical trajectory of $N \in \mathbb{N}$ samples $X_N = \{u_n\}_{n=0}^{N-1} \subset X$ with $u_n = \Phi^n(u_0)$, $u_0 \in X$, and the associated sampling measure $\mu_N = \sum_{n=0}^{N-1} \delta_{u_n} / N$. The space of observables is defined as the NM -dimensional Hilbert space $H_N = L^2(\Omega, \sigma_N)$ with product measure $\sigma_N = \mu_N \times \nu_M$. To construct our closure model we require access to the resolved state samples $\hat{u}_n = \text{proj}_r(u_n) \in X_r$ and associated flux samples $f_j(u_n, \cdot) \in L^2(S, \nu_m)$, $j \in \{0, \dots, d-1\}$. We denote the product state samples by $\omega_{nm} = (u_n, x_m) \in \Omega_{NM}$ with $u_n \in X_N$ and $x_m \in S_M$. We operate under the assumption that the sampling measures μ_N converge weakly to the invariant measure μ , in the sense that $\lim_{N \rightarrow \infty} \int_X f d\mu_N = \int_X f d\mu$ for all $f \in C_b(X)$ [13].

In the discrete setting the kernel integral operator $K_N: H_N \rightarrow H_N$ corresponding to (7) is defined as

$$K_N f = \int_{\Omega} k(W_Q(\cdot), W_Q(\omega)) f(\omega) d\sigma_N(\omega) = \frac{1}{NM} \sum_{n=0}^{N-1} \sum_{m=0}^{M-1} k(W_Q(\cdot), W_Q(\omega_{nm})) f(\omega_{nm}). \quad (12)$$

Using the L leading eigenfunctions $\{\phi_\ell\}_{\ell=0}^{L-1}$ of K_N we construct the L -dimensional subspace $H_N^L \subset H_N$ as their linear span. Computing the eigenfunctions of K_N with a direct method has a computational cost that scales with $(NM)^3$, making the computation prohibitively expensive as NM grows. To make the computation more tractable, in our numerical experiments we build a low rank approximation of the kernel matrix \mathbf{K}_N associated with K_N and use it to compute its eigenfunctions with reduced cost (Section 3.3). In what follows, we make use of the orthogonal projection $\text{proj}_L: H_N \rightarrow H_N^L \subset H_N$ to project an operator $A \in B(H_N)$ to $\text{proj}_L A \text{proj}_L \in B(H_N^L)$, which can then be represented by an $L \times L$ matrix of coefficients with respect to our basis.

Each flux function $f_j \in H_N$ corresponds to a vector in \mathbb{R}^{NM} with entries $f_j(u_n, x_m)$, where $u_n \in X_N$ and $x_m \in S_M$. Every such function is used to define a multiplication operator $\tilde{A}_j \in B(H_N)$ and, after orthogonal projection, form a quantum observable $A_j \in B(H_N^L)$, which is generally no longer a multiplication operator. Using our orthonormal basis, each A_j is represented by an $L \times L$ matrix \mathbf{A}_j with entries $A_{j,ik} = \langle \phi_i, \tilde{A}_j \phi_k \rangle_N$.

The discretization process employed by QMCl to generate the observables A_j is positivity preserving. This means that if f_j is a sign definite function (positive or negative), then so will be the resulting observable A_j , producing surrogate fluxes that agree in sign with the true fluxes. This is one of the main benefits of mapping classical observables and density functions to their associated operators before discretizing them with respect to our basis. This is in contrast to discretizing the functions directly, which does not guarantee the preservation of their positivity, potentially leading to surrogate fluxes that differ in sign from the true ones. Of course, this benefit is accompanied by an increase in computational cost, since every observable is represented by a matrix of coefficients with respect to our basis, instead of a vector of coefficients.

To model the unresolved degrees of freedom we form a field of quantum density operators $\rho: S_M \rightarrow B(H_N^L)$, consisting of one density operator $\rho_m = \rho(x_m) \in B(H_N^L)$ for each gridpoint $x_m \in S_M$. Each density operator ρ_m is constructed as the projection along a real valued function $h_m \in H_N^L$, $\rho_m = \langle h_m, \cdot \rangle_N h_m$. Taking advantage of its rank-one structure, each ρ_m is represented by the coefficient vector $\boldsymbol{\rho}_m \in \mathbb{R}^L$ with entries $\rho_{m,\ell} = \langle \phi_\ell, h_m \rangle_N$.

Having formed the quantum observables and density operators, we are now in a position to formulate the calculation of the required surrogate fluxes. For each $j \in \{0, \dots, d-1\}$ we define the surrogate flux function $\tilde{f}_j: S_M \rightarrow \mathbb{R}$, which uses the quantum observable A_j and field of density operators ρ to produce the surrogate fluxes $\tilde{f}_j(x_m) = \text{tr}(\rho(x_m) A_j) \in \mathbb{R}$ at each gridpoint $x_m \in S_M$. Using our basis representation this corresponds to $\tilde{f}_j(x_m) = \boldsymbol{\rho}_m^\top \mathbf{A}_j \boldsymbol{\rho}_m$.

The time evolution of the quantum density operators under the dynamics is carried out using the projected transfer operator $P_N^L: B(H_N^L) \rightarrow B(H_N^L)$. To build P_N^L we begin by defining the shift operator $P_N: H_N \rightarrow H_N$

$$P_N f(\hat{u}_n, x_m) = \begin{cases} 0 & \text{if } n = 0 \\ f(\hat{u}_{n-1}, x_m) & \text{if } 1 \leq n < N. \end{cases}$$

After orthogonal projection we obtain P_N^L and its $L \times L$ coefficients matrix \mathbf{P}_N^L . Given a quantum density operator $\rho_n(x_m)$ at time t_n with vector representation $\boldsymbol{\rho}_n$ we obtain the updated state $\boldsymbol{\rho}_{n+1}$ by

$$\boldsymbol{\rho}_{n+1} = \frac{\mathbf{P}_N^L \boldsymbol{\rho}_n}{\|\mathbf{P}_N^L \boldsymbol{\rho}_n\|_2}$$

where the renormalization is performed because the matrix \mathbf{P}_N^L is generally not orthogonal.

Finally, we arrive at the bayesian conditioning of quantum density operators. Each density operator ρ_m is conditioned by a quantum effect operator $e_m \in B(H_N^L)$ formed based on a given product state vector $\omega_m = (u, x_m)$. To build e_m from ω_m we use the conditioning kernel function $\kappa_c: \Omega \times \Omega \rightarrow \mathbb{R}$,

$\kappa_c(\omega, \omega') = k_c(W_J(\omega), W_J(\omega'))$ which acts by composition of a gaussian kernel function $k_c: \mathbb{R}^J \times \mathbb{R}^J \rightarrow \mathbb{R}$ and an embedding map $W_J: \Omega \rightarrow \mathbb{R}^J$ with parameter $J \in \mathbb{N}$. The map W_J returns the resolved state component of the J nearest spatial neighbors of ω_m in a specified order. For example, for a one dimensional grid and odd J its action is given by

$$W_J((u, x_m)) = (\text{proj}_r(u)(x_{m-(J-1)/2}), \dots, \text{proj}_r(u)(x_m), \dots, \text{proj}_r(u)(x_{m+(J-1)/2})).$$

This can be generalized analogously for higher dimensional grids. The gaussian kernel k_c then acts by

$$k_c(W_J(\omega), W_J(\omega')) = \exp\left(-\frac{1}{\epsilon' J} \|W_J(\omega) - W_J(\omega')\|^2\right) \quad (13)$$

where $\|\cdot\|$ denotes the euclidean norm in \mathbb{R}^J and $\epsilon' > 0$ a bandwidth parameter. Note that the bandwidth parameter ϵ' is different from the one introduced earlier in kernel (9); it can again be selected using the tuning procedure developed in [34]. In our numerical experiments we employ the above kernel using a variable bandwidth; details on this construction and an algorithm for computing the variable bandwidth can be found in [37, 38].

For the given product state vector ω_m , we use the kernel κ_c and the full training dataset Ω_{NM} to produce the function $f_m \in H_N$, $f_m(\cdot) = \kappa_c(\omega_m, \cdot)$, which compares the vector ω_m with every other product state vector included in our training dataset. Intuitively, the function f_m can be thought of as a similarity function on the dataset Ω_{NM} , measuring how “similar” the given state ω_m is to the states included in Ω_{NM} . Because kernel κ_c acts by composition with W_J , it compares the nearest spatial neighbors of ω_m with the nearest neighbors of every other available state vector, mimicking the structure of the stencil used for the spatial discretization of the considered dynamics. This makes for a stronger similarity condition than comparing values of states at only a single gridpoint, forcing the kernel to be more selective in the states it considers to be dynamically similar to the given ω_m .

Next, we use the square root $f_m^{1/2}$ to form a multiplication operator and, after orthogonal projection, the desired quantum effect $e_m \in B(H_N^L)$. This is then used to condition the prior density operator ρ_m via the quantum Bayes rule (4), thereby creating the posterior density operator $\rho_m|_{e_m}$ that encodes the state space similarities captured by f_m . Based on our basis representation, this operation takes the form

$$\rho_m|_{e_m} = \frac{e_m \rho_m}{\|e_m \rho_m\|_2}$$

where e_m denotes the $L \times L$ matrix of coefficients of effect e_m . We refer to the map $\omega_m \mapsto e_m$ as the *feature map* and to f_m as the *feature vector* produced by kernel κ_c from the product state vector ω_m . Explanation for why we use the square root of the feature vector $f_m^{1/2}$ instead of f_m to build e_m is given in [13].

Using the procedure outlined above, the density operator $\rho_m = \rho(x_m)$ associated with every point x_m on our grid can be conditioned based on the corresponding product state vector (u, x_m) . That is, given a new state vector $u \in X$, the density operator ρ_m is conditioned based on the spatially local information $\omega_m = (u, x_m)$, by comparing this product state vector to every other product state vector available in our training dataset. Because the spatially local value ω_m is used for the conditioning process (rather than the full state u), spatial translations of the state u are naturally factored during the conditioning process. This means that if a spatial translation of the state u is present in our training dataset, then the similarity between the product state ω_m and the corresponding value of the spatial translation of u will be identified in the conditioning process. For PDEs with spatial translation symmetry, this means that we do not have to artificially inflate our training dataset by including all spatial translations of the sampled states.

2.6. Multi-trajectory data

In the previous section we presented the data based implementation of our closure scheme using a single dynamical trajectory as our training dataset. In this section we generalize this construction to the case where the training dataset consists of multiple trajectories. We begin by motivating the use of multiple trajectories, before presenting the modifications required in the theoretical and data based formulations of the scheme.

Using a single dynamical trajectory is generally sufficient when considering a dynamical system possessing a unique physical measure, namely a measure that can be sampled by a set of initial conditions of positive measure with respect to the ambient measure [39, 40]. Using multiple trajectories is of interest when considering dynamical systems possessing multiple physical measures; for instance, hamiltonian systems or hyperbolic systems with several competing basins of attraction. Additionally, using multiple trajectories is necessary in the forecasting of parameter dependent systems, whose qualitative dynamics changes with respect to a bifurcation parameter. Finally, even in systems with a unique physical measure, being able to use multiple trajectories allows one to consider optimal sampling strategies. In designing such a strategy one tries to optimize the sampling rate with respect to a chosen objective, instead of relying on the inherent rate provided by a single trajectory.

For example, in Section 3 we will consider an application of our scheme to a closure problem for the shallow water equations (14), a hyperbolic, energy conservative system of PDEs. Depending on the initial condition, the solution trajectory of equations (14) can reach different limit sets, since there is no dissipation to focus the global dynamics to a lower dimensional subset of its state space. As such, using several trajectories becomes important, allowing us to sample different limit sets of the dynamics.

We consider a finite collection of $I \in \mathbb{N}$ invariant probability measures $\{\mu_i\}$ on X with mutually disjoint supports, $i \in \{0, \dots, I-1\}$, and define the invariant probability joint measure $\mu = \sum_{i=0}^{I-1} \mu_i / I$ as their average. By construction, the Hilbert space of observables $H = L^2(\Omega, \mu \times \nu_M)$ admits the decomposition $H \simeq \bigoplus_{i=0}^{I-1} H_i$ with component spaces $H_i = L^2(\Omega, \mu_i \times \nu_M)$, where the isomorphism is up to a rescaling of the inner products of H_i by the factor $1/I$. Our data based formulation mirrors the one presented in Section 2.5, while also taking advantage of the decomposition of H into its component subspaces.

We generate the finite sampled trajectories $\{u_n^{(i)}\}_{n=0}^{N_i-1}$ of $N_i \in \mathbb{N}$ samples each, where $i \in \{0, \dots, I-1\}$ as above. Each trajectory gives rise to its associated empirical sampling measure $\mu_{i, N_i} = \sum_{n=0}^{N_i-1} \delta_{u_n^{(i)}} / N_i$, where we assume that each sampling measure μ_{i, N_i} converges to μ_i in the weak-* sense as $N_i \rightarrow \infty$. Denoting $N = \sum_{i=0}^{I-1} N_i$, we define the Hilbert space $H_N = L^2(\Omega, \mu_N \times \nu_M)$ with the joint sampling measure $\mu_N = \sum_{i=0}^{I-1} \mu_{i, N_i} / I$. Since the individual trajectories are assumed to be mutually disjoint, we have the analogous decomposition $H_N \simeq \bigoplus_{i=0}^{I-1} H_{N_i}$.

Leveraging the decomposition of H_N , we use each individual trajectory and the approach described in Section 2.5 to build an eigenfunction basis for each component space H_{N_i} separately. Relying on the $L_i \in \mathbb{N}$ leading eigenfunctions, we then form the subspace $H_{N_i}^{L_i} \subset H_{N_i}$. Denoting $L = \sum_{i=0}^{I-1} L_i$, we define the combined space $H_N^L = \bigoplus_{i=0}^{I-1} H_{N_i}^{L_i}$, with the direct sum of the component bases producing a basis for the combined space.

The basis of H_N^L derived in this way consists of a total of L elements, each being an eigenfunction of a block diagonal operator $K_N = K_{N_0} \oplus \dots \oplus K_{N_{I-1}}$ with the component kernel integral operators K_{N_i} in its diagonal blocks. More specifically, each component basis vector $\phi_\ell^{(i)}$ represents the values of a function on N samples, with all of its values being zero except for the block of values that corresponds to the N_i samples of the i th trajectory it was derived from. This approach has lower computational cost, as it requires that we solve a total of I eigenvalue problems for an $N_i \times N_i$ matrix each, instead of a single eigenvalue problem for an $N \times N$ matrix. However, our approach also requires that each component measure μ_i is individually adequately sampled, as opposed to adequate joint sampling of measure μ .

Having derived the basis for space H_N^L , the construction of the rest of the scheme proceeds as in Section 2.5. The only additional difference is in the definition of the shift operator P_N , where time shifts are now applied only *within* each trajectory, and the first temporal sample of each trajectory is mapped to zero. Namely, we make sure not to shift samples *across* different trajectories.

After forming our QMC1 closure model in H_N^L , our goal is to use it to predict the dynamics of a chosen dynamical system for out of sample initial conditions; namely, initial conditions lying outside of the basins of the component measures μ_i sampled in the training stage.

3. Application

The shallow water equations govern the motion of an incompressible fluid when its vertical length scale can be considered negligible compared to its horizontal length scale. The equations are derived from the conservation laws for mass and momentum, with various forms finding applications in areas such as ocean dynamics, often incorporating additional terms modeling the effects of bottom topography and Coriolis force [41, 42].

We consider the shallow water equations on a bounded one dimensional spatial domain S with periodic boundary conditions. The system of equations governs the evolution of the water height h and momentum $q = hv$ fields, with v denoting the velocity field. The governing equations read

$$\begin{aligned} \partial_t h + \partial_x q &= 0 \\ \partial_t q + \partial_x (q^2/h + 1/2Fr^{-2}h^2) &= 0 \end{aligned} \tag{14}$$

subject to an appropriate initial condition. In the above ∂_t and ∂_x denote differentiation with respect to time and space respectively, while Fr denotes the flow's Froude number, which is a dimensionless ratio of inertial over gravitational forces. Using the state variable $u = (h, q) \in X \subset L^2(S, \nu; \mathbb{R}^2)$ and function $f(u) = (q, q^2/h + 1/2Fr^{-2}h^2)$ we rewrite (14) in the compact form

$$\partial_t u + \partial_x f(u) = 0. \tag{15}$$

In addition to its applications in ocean dynamics, the shallow water equations problem (15) has additional properties that make it a good test case for our QMCI closure framework. First, the dynamics governed by (15) is equivariant under the actions of the spatial translation group on S . Second, forming a training dataset that is sufficiently representative of a range of its dynamics requires the use of multiple dynamical trajectories. Third, previous works have considered various closure schemes for variations of (15), demonstrating the amenability of the equations to closure problems that arise from spatial coarsening [43, 44]. In particular, our discretization and coarsening methodology is based on [44]. Finally, the equations act as a good idealized model for more complex nonlinear hyperbolic PDEs that are prevalent in fluid and plasma dynamics modeling.

3.1. Discretization

We employ a finite volume spatial discretization of (15) using a uniform fine grid of $M_f \in \mathbb{N}$ cells with length $\Delta x = L/M_f$ each, centered at points $x_m \in S$, $m \in \{0, \dots, M_f - 1\}$. We use $S_f = \{x_m\}_{m=0}^{M_f-1} \subset M$ to denote the center points of the fine discretization cells. The cell averaged state variables u_m , $m \in \{0, \dots, M_f - 1\}$, are defined by taking the spatial average of the original state function u over the cell centered at x_m . Without misunderstanding, we reuse the same symbol u to denote the averaged state variables, which can be represented by the vector $\mathbf{u} \in \mathbb{R}^{2M_f}$ for every time $t \geq 0$.

The temporal evolution of the fine state variables u_m is governed by the system of equations

$$\dot{u}_m = \frac{1}{\Delta x} (F_m - F_{m+1}) \tag{16}$$

using the local Lax-Friedrichs (LLF) numerical flux

$$F_m = \frac{1}{2} [f(u_{m-1}) + f(u_m)] - \frac{\lambda_m}{2} (u_m - u_{m-1}) \tag{17}$$

with

$$\lambda_m = \max (|q_{m-1}/h_{m-1}| + Fr^{-1}\sqrt{h_{m-1}}, |q_m/h_m| + Fr^{-1}\sqrt{h_m}). \tag{18}$$

In the above, subscripts denote components of the associated vectors while F_m denotes the numerical flux at the left face of the cell centered at $x_m \in S_f$ [45]. Based on (17) and (18) we introduce the notation

$$F_m = \mathcal{F}_{LLF}(u_{m-1}, u_m)$$

which will be used later on to define the coarse grid fluxes.

We now form a coarse grid and associated coarse state variables defined as local spatial averages of the fine variables u_m . In particular we form $M_c \in \mathbb{N}$ coarse grid cells by merging every $M_s \in \mathbb{N}$ fine cells; in this way, $M_c = M_f/M_s$ and each coarse cell has length $\Delta\hat{x} = M_s\Delta x$. We define the resulting coarse grid $S_c = \{\hat{x}_m\}_{m=0}^{M_c-1} \subset S$, $m \in \{0, \dots, M_c - 1\}$, representing the center points of the coarse grid cells. Each coarse grid state variable \hat{u}_m is defined as the average of the fine state variables included within its associated coarse grid cell. The coarse variables are represented by the vector $\hat{\mathbf{u}} \in \mathbb{R}^{2M_c}$ for every time $t \geq 0$. Their temporal evolution is governed by the system of equations

$$\dot{\hat{u}}_m = \frac{1}{\Delta\hat{x}}[(\hat{F}_m + G_m) - (\hat{F}_{m+1} + G_{m+1})] \quad (19)$$

with coarse grid fluxes

$$\hat{F}_m = \mathcal{F}_{LLF}(\hat{u}_{m-1}, \hat{u}_m) \quad (20)$$

and subgrid fluxes

$$G_m = F_{M_s m} - \hat{F}_m. \quad (21)$$

The system (19) is equivariant under the actions of the discrete group of spatial translations on S_c .

By definition, the coarse grid fluxes (20) depend only on the coarse variables. On the contrary, the subgrid fluxes (21) depend on both the coarse and the original fine variables; in particular, they depend on the values of u_m in the fine cells that border the interfaces of each coarse cell. For the physical system considered, the subgrid fluxes act as antidiffusive corrections to the coarse grid fluxes, increasing the accuracy of the discretization compared to one performed entirely on the coarse grid [44].

The temporal discretization of evolution equations (16) and (19) is carried out using the modified Euler method (two-stage Runge-Kutta), which has favorable structure preservation properties for the present problem [44]. In what follows, we consider the coarse grid variables as the resolved degrees of freedom and the discrete time version of (19) as the equation generating the resolved dynamics. To close the system of equations we need to provide a closure model that can infer the subgrid fluxes G_m from the resolved variables \hat{u}_m , thereby removing the explicit dependence on the original fine grid variables u_m .

3.2. Closure model

To generate our training dataset and be able to compare our surrogate model with a reference model acting as the ground truth, we approximate the “true” shallow water dynamics by the discrete time version of the fine grid dynamics (16). As such, the full state space of the dynamics is a Hilbert subspace of the set of L^2 functions on the grid produced by our fine discretization. More specifically we set $X \subset L^2(S, \nu_f; \mathbb{R}^2)$, where ν_f denotes the restriction of the Lebesgue volume measure ν to the σ -algebra generated by the fine discretization cells.

As mentioned in the previous section, we consider the coarse grid variables as our resolved degrees of freedom. Therefore, we define the resolved state space $X_r = L^2(S, \nu_c; \mathbb{R}^2) \cap X$ and decompose the full state space as $X = X_r \oplus X_u$, with unresolved state space $X_u = X_r^\perp$. In the definition of X_r , the measure ν_c corresponds to the restriction of ν to the σ -algebra of sets generated by the coarse discretization cells. As a result, the resolved state space can be considered as a space of piecewise constant functions, each taking a constant value on each cell formed by the coarse discretization. With these choices in place, the full dynamics $\Phi^{n\Delta t}$ is given by the discrete time version of (16) and the resolved dynamics $\Phi_r^{n\Delta\hat{t}}$ by the discrete time version of (19), with $n \in \mathbb{N}$ and respective timesteps $\Delta t > 0$ and $\Delta\hat{t} = M_s\Delta t$.

We define the product state space $\Omega = X \times S$ and the Hilbert space of observables $H_N = L^2(\Omega, \sigma_N)$, with total number of samples $N \in \mathbb{N}$ and measures $\sigma_N = \mu_N \times \nu_M$ and $\nu_M = \nu_c$. For notational consistency with the previous sections, from now on we denote by $M = M_c$ the number of coarse grid cells and by $S_M = S_c \subset S$ the set of gridpoints representing the coarse grid cells. We introduce two flux functions $f_j \in H_N$, $j \in \{0, 1\}$, producing the fluxes for the height and momentum variables respectively, and denote their collection by $f = \{f_j\}_{j=0}^1$. For every state $u \in X$ the associated fluxes $f_j(u)$ are given by (21).

Using the full dynamics (16) we generate N samples of the resolved state variables $\{\hat{u}_n\}_{n=0}^{N-1}$ and the fluxes $\{f(u_n, \cdot)\}_{n=0}^{N-1}$, which will be used as our training data and may consist of one or more dynamical

trajectories. Each sample \hat{u}_n or $f(u_n, \cdot)$ is represented by a vector in \mathbb{R}^{2M} holding the values corresponding to the height h and momentum q variables in each coarse grid cell.

To form our closure model we define a field of quantum density operators $\rho: S_M \rightarrow B(H_N)$ and two quantum observables $A_j \in B(H_N)$, $j \in \{0, 1\}$. Each density operator $\rho(x_m)$ will be used to model in a statistical sense the unresolved variables in the coarse grid cell centered at $x_m \in S_M$. From the two quantum observables, observable A_0 will be used to produce the surrogate fluxes for the height h variables and is defined as multiplication by the true flux function f_0 ; analogously, observable A_1 will produce the surrogate fluxes for the momentum q variables and is defined as multiplication by f_1 . With these definitions in place, the surrogate fluxes are computed using the two surrogate flux functions $\tilde{f}_j: S_M \rightarrow \mathbb{R}$ with action $\tilde{f}_0(x_m) = \text{tr}(\rho(x_m)A_0)$ and $\tilde{f}_1(x_m) = \text{tr}(\rho(x_m)A_1)$ for every $x_m \in S_M$.

In Appendix A we list the sequence of steps used to build the data based QMCI model and apply it to predict the dynamics based on a given initial condition.

3.3. Numerical results

We consider the shallow water equations (15) on the spatial domain $S = [-25, 25]$ with Froude number $Fr = 1/\sqrt{2g}$, where g denotes the acceleration of gravity. We perform the spatial discretization using a fine grid of $M_f = 1920$ cells and the temporal discretization using the midpoint Euler method with timestep $\Delta t = 0.1\Delta x$, where Δx is the length of each fine cell.

Training

We define the one-parameter family of initial conditions

$$\begin{aligned} h_0(x) &= 1 + 0.3(1 - \delta/2) \sin\left(\frac{2\pi}{L_S} 3.5(1 - \delta/2)x + \pi/6\right) \\ v_0(x) &= 1 + 0.2(1 - \delta) \sin\left(\frac{2\pi}{L_S} 3(1 - \delta)x\right) \end{aligned} \tag{22}$$

with $x \in S$, $L_S = 50$, parameter $\delta \in [0, 1]$, h_0 the initial condition for height and $q_0 = h_0 v_0$ the initial condition for momentum. The solutions generated by this family of initial conditions feature a number of wave fronts traveling in different directions and interacting with one another. Figures 2 and 3 present space-time heatmaps of the solutions that will be used to test the predictive performance of our closure model.

Using the assumptions and methodology introduced in Section 2.6 for dealing with training data consisting of multiple trajectories, we consider μ to be the invariant measure generated by the full dynamics (16) restricted to the family of initial conditions (22) for $\delta \in [0, 1]$. To sample this measure we use three trajectories generated using the values $\delta \in \{0, 0.5, 1\}$. For each trajectory we integrate the full dynamics (16) in time for 12,200 timesteps and then sample the next 3,260 timesteps. Each sample contains the values of functions h and q on the fine grid.

To derive the resolved state samples that will be used as our training data, we spatially average the collected samples. By averaging the state data over every $M_s = 20$ fine cells we arrive at a coarse grid of $M = 96$ cells of length $\Delta \hat{x} = 20\Delta x$ each. Given that each cell is now 20 times longer, we also increase the sampling timestep by the same amount to set $\Delta \hat{t} = 20\Delta t$. From the original 3,260 samples per trajectory generated on the fine grid, we keep every 20th sample, leading to 163 samples per trajectory. For each one of those samples we spatially average the solution over every 20 cells to derive our resolved state samples, namely the averaged values of h and q over the coarse grid. We then derive the subgrid flux training samples using (21).

Using $Q = 64$ delays, these samples yield 100 training samples per trajectory in delay embedded form, adding up to $N = 300$ samples in total. Each resolved state sample consists of $2M = 192$ values, 96 for each of the height and momentum variables. With this training dataset, the dimension of the product Hilbert space H_N is equal to $NM = 28800$. Employing the approach described in Section 2.6 we build an orthonormal basis $\{\phi_\ell\}_{\ell=0}^{L-1}$ with a total of $L = 6144$ eigenfunctions and define H_N^L as their linear span. Each eigenfunction is represented by a vector in \mathbb{R}^{NM} . Finally, we set $J = 5$ to define the stencil map W_J that

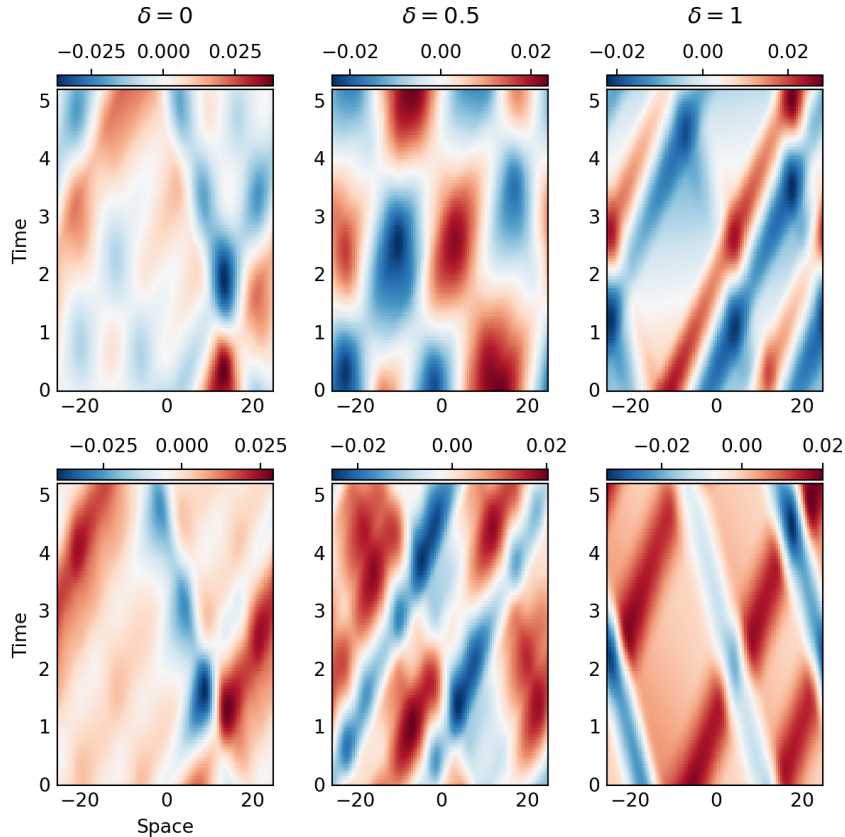


Figure 1: Space-time heatmaps depicting two eigenfunctions ϕ_ℓ of the kernel integral operator \mathbf{K}_N from (12) for each of the three trajectories used as our training data. The top row shows the third eigenfunction for each of the three trajectories; the bottom row the fourth eigenfunction for each trajectory. From left to right, the first column corresponds to the trajectory data obtained for $\delta = 0$, the second to $\delta = 0.5$ and the third to $\delta = 1$.

will be used for the bayesian conditioning of the quantum density operators. The data based realization of the closure model developed in Section 3.2 will take place in the constructed subspace H_N^L .

The number of delays Q was chosen by a combination of physical reasoning and trial and error to balance the effectiveness of the derived basis in representing the true flux samples and the cost associated with its computation. A useful rule of thumb is to select a delay window that is comparable to the dominant timescale of the physical processes of interest. In our case, we see that the traveling wave fronts interact approximately every 30 timesteps (≈ 1.5 time units) for the solution in Figure 2, and approximately every 50 timesteps (≈ 2.5 time units) for the solution in Figure 3, with similar results for additional solutions not shown here. Using $Q = 64$ timesteps is sufficient to ensure that at least one period of this interaction is captured in each delay embedded sample. Additionally, increasing the value of Q further did not lead to noticeable differences in our results. The stencil size J used for the conditioning of the quantum density operators was chosen empirically. Increasing the value of J further was shown to slightly improve the performance of the bayesian conditioning, but with an associated increase in computational cost.

To form the orthonormal basis $\{\phi_\ell\}_{\ell=0}^{L-1}$ we must compute the eigenvectors of the $NM \times NM$ symmetric kernel matrix \mathbf{K}_N representing the operator (12). To reduce the computational cost of this operation we perform a partial Cholesky factorization of \mathbf{K}_N to approximate it by a lower rank matrix $\tilde{\mathbf{K}}_N = \mathbf{F}\mathbf{F}^T$ with $\mathbf{F} \in \mathbb{R}^{NM \times r}$ and $r < NM$. We perform the factorization using the rank parameter $r = L = 6144$ and the randomized algorithm developed in [46]. We then use the approximate kernel matrix to perform its

bistochastic normalization and solve the eigenvalue problem with reduced cost [31].

A selection of the resulting eigenfunctions is presented in Figure 1, where we show two eigenfunctions for each of the three trajectories used to build our training dataset. The shown eigenfunctions exhibit propagating fronts which resemble the main features of the true state and flux samples presented in Figures 2 and 3. More specifically, they are approximately constant on the characteristic lines of the propagating wave fronts, as expected from their symmetry invariance property. Similar features are present in the rest of the eigenfunctions not shown here. As explained in Sections 2.3 and 2.4, the strong dynamical relevance of each eigenfunction is a result of its dynamical symmetry invariance and of the fact that generally it cannot be represented as the tensor product of a single pair of spatial and temporal modes. These properties allow us to compute a compressed representation of the true dynamics with a moderate number of eigenfunctions, enhancing the computational efficiency of the resulting closure scheme.

Prediction

To test the predictive performance of the surrogate model derived by QMCI we use two initial conditions obtained from (22) for $\delta \in \{0.25, 0.75\}$, which are trajectories not included in the training dataset. After integrating the true dynamics (16) for 12,200 timesteps we spatially average the found solutions to generate the initial conditions that will be used to initialize the resolved state in QMCI. Using those initial conditions we integrate in time the coarse dynamics (19) using timestep $\Delta\hat{t}$ and the subgrid fluxes predicted by QMCI. In what follows, we present results obtained after integrating for a total of 120 timesteps, while performing the bayesian conditioning of the quantum density operators every 10 timesteps.

The results comparing the evolution under the true and surrogate models are grouped into four figures. Figures 2 and 4 include the results for the trajectory generated by the initial condition obtained from (22) for $\delta = 0.25$. Figures 3 and 5 showcase the results obtained for $\delta = 0.75$.

Looking at the heatmaps for the height and momentum fields in Figure 2 for the trajectory with $\delta = 0.25$ and in Figure 3 for the one with $\delta = 0.75$, we see that QMCI clearly captures the main features of the dynamics for the tested time horizon. For both trajectories, QMCI correctly predicts the main traveling wave features of the dynamics, including the spatial variations of the waves as they interact with one another. Moreover, the magnitude of the predicted fields is consistent with the true dynamics in most regions of the spatial domain. In addition to the results shown in these figures, we have also verified that QMCI can reproduce the dynamical trajectories included in its training dataset with good accuracy.

In the present closure model, the subgrid fluxes play the role of antidiffusive corrections to the fluxes generated entirely on the coarse grid [44]. Their values are proportional to the spatial derivative of the associated field, taking large values when the height or momentum field is changing rapidly in space, and approximately zero value when the fields are constant in space. As a result, the contribution of the subgrid fluxes is critical in regions of strong spatial variation of the height and momentum fields, counterbalancing the increased diffusion of the solution introduced by our coarsening of the original dynamics by spatial averaging. The strong spatial variation of the true subgrid fluxes renders the considered dynamics challenging to resolve and predict accurately by any closure scheme (Section 3.4). Typically, when the exact value of the subgrid fluxes is not predicted correctly by the employed closure model (derived by QMCI or another method), the surrogate evolution will be more diffusive than the true evolution.

The effect of diffusion can be seen in the heatmaps for the two trajectories. By comparing the true and predicted fields of height and momentum, we see that the surrogate dynamics involves stronger diffusion of the solution in areas where there is strong spatial variation. The increased diffusion is seen in the plots as bleeding of color between different space-time regions, with the boundaries between those regions being less sharp than in the true dynamics. Similarly, the same effect can be seen by comparing the subgrid flux fields for height and momentum. In the true dynamics, the peaks of the fluxes are sharp and clearly separated from the valleys, with clearly visible waves traveling in opposite directions. In the predicted dynamics, although the waves are still predicted correctly, their peaks are not as sharp, with their values diffusing more strongly to the surrounding region.

The subgrid flux plots also clearly demonstrate the effect of the bayesian conditioning of the quantum density operators, which for these results is performed every 10 timesteps (≈ 0.5 time units). One can see the discontinuities that occur every 10 timesteps for the predicted fluxes over large regions of the spatial domain.

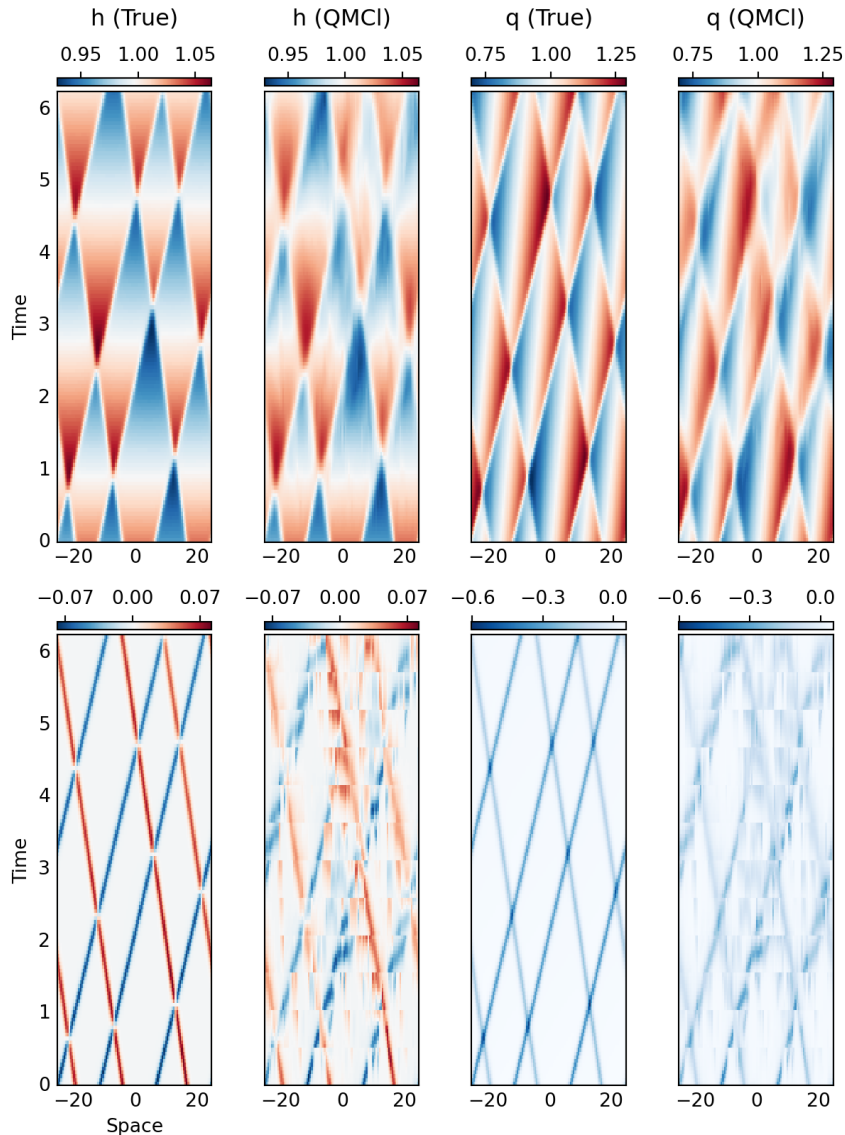


Figure 2: Space-time heatmaps for the trajectory with $\delta = 0.25$. The top row shows the results for the resolved state variables; the bottom row for the subgrid fluxes. For each row, from left to right: the first two plots show the results for the height field h , with the true results on the left and the predicted results on the right; the next two plots show the results for the momentum field q , with true results on the left and predicted on the right.

These discontinuities represent corrections introduced to the predicted flux values every time conditioning of the density operators is performed. We perform the bayesian conditioning every 10 timesteps to reduce the computational cost of the simulation, since the conditioning is one of the most expensive operations in our closure scheme (Section 3.4). In general, the prediction accuracy increases with increased conditioning frequency. Based on our numerical experiments, conditioning the density operators every 10 timesteps strikes a good balance between prediction accuracy and computational cost for the considered dynamics.

Similar conclusions can be drawn from the spatial profiles shown in Figure 4 for the trajectory with $\delta = 0.25$ and Figure 5 for that with $\delta = 0.75$. In these plots one can see that the subgrid fluxes are proportional to the spatial derivative of the associated field, leading to sharp variations in space. The

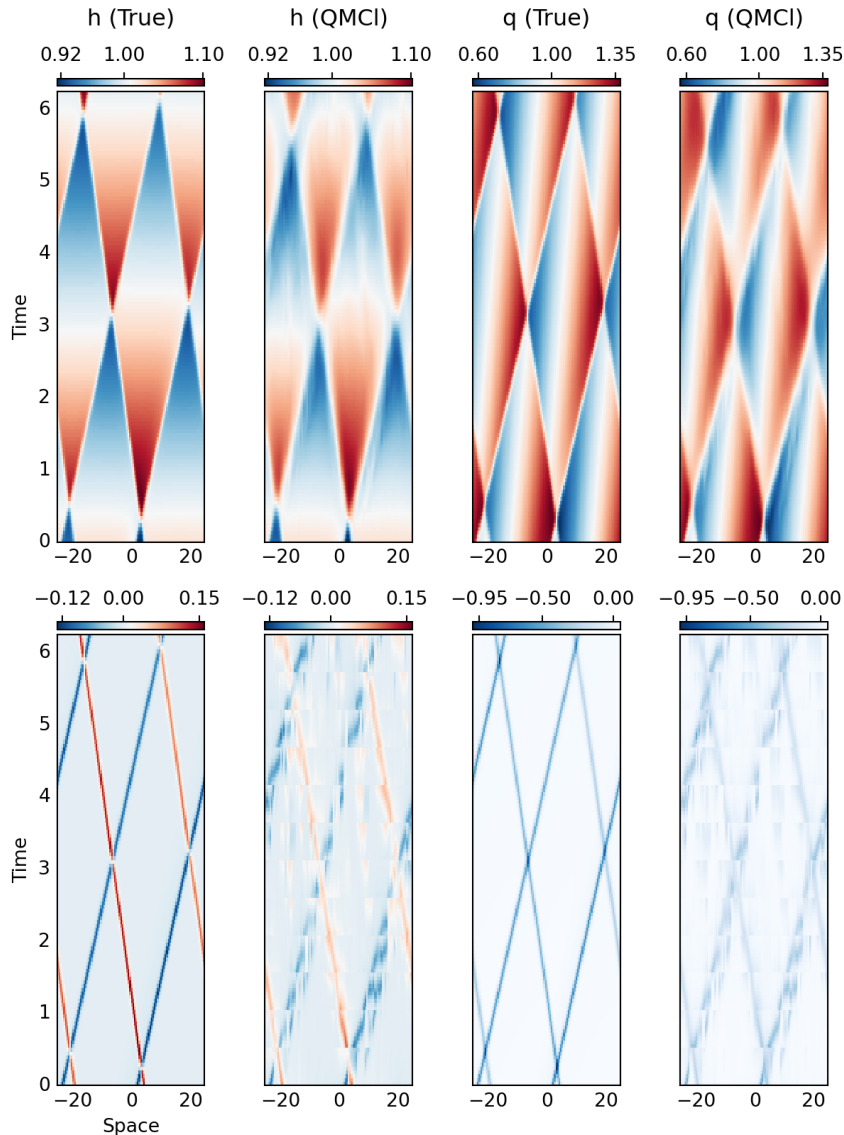


Figure 3: Space-time heatmaps for the trajectory with $\delta = 0.75$. The layout of the plots is as in Figure 2.

predicted dynamics preserves the main features of the true fields, but struggles to capture the sharp peaks of the subgrid fluxes, leading to stronger diffusion of the height and momentum fields in regions of strong spatial variation.

To further demonstrate the crucial role played by the subgrid fluxes in counterbalancing diffusion, in Figure 6 we compare the evolution of the QMCI surrogate dynamics with the true dynamics generated entirely on the coarse grid, namely with the subgrid fluxes (21) set to zero. The comparison is carried out for the trajectory generated from the initial condition (22) with $\delta = 0.25$ (Figures 2 and 4), but similar conclusions can be drawn from other initial conditions. The comparison demonstrates that the surrogate fluxes predicted by QMCI successfully counteract the diffusive effect of the spatial coarsening seen in the coarse grid simulation for the tested time horizon. Namely, although the subgrid fluxes predicted by QMCI are not as accurate as the true subgrid fluxes in regions of strong spatial variation of the solution, they

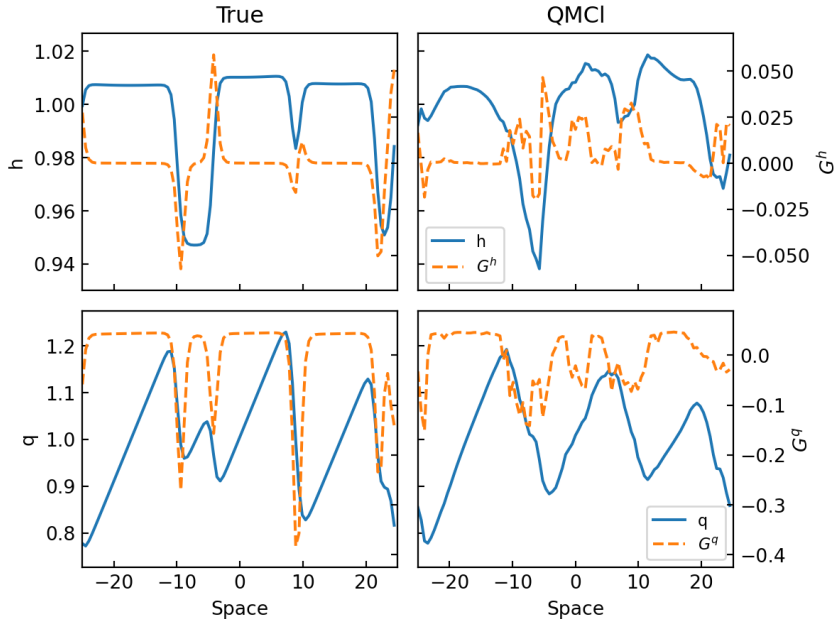


Figure 4: Spatial profiles of the final solution snapshot for the trajectory with $\delta = 0.25$. The top row shows the results for the resolved state and the subgrid fluxes for the height field h ; the bottom row for the momentum field q . In each row, the true results are on the left subplot, the predicted ones on the right subplot. Within each subplot, full lines are used for the resolved state, with their numerical values indicated on the left axis; dashed lines are used for the subgrid fluxes, with their values indicated on the right axis.

are nevertheless effective in counterbalancing diffusion and thus improving the accuracy of the predicted dynamics.

3.4. Discussion

In the following paragraphs we discuss several aspects of the presented closure scheme and how they inform future research directions.

Computational aspects

Extending the QMCI framework to spatiotemporal dynamics comes with the challenge of increased computational cost for its implementation, primarily due to the increased size of the training dataset required to capture the main features of dynamics that evolves in both space and time. One key area of focus for future work is reducing the cost of the numerical implementation of QMCI and improving its scaling with the number of temporal samples N , grid size M and spectral resolution L .

In the offline stage, the most expensive operation is computing the leading L eigenfunctions of the $NM \times NM$ symmetric kernel matrix \mathbf{K}_N representing the kernel integral operator (12). Even for moderate size parameters N and M , solving such an eigenvalue problem can quickly become very expensive. As explained in Section 3.3, to address this we performed a partial Cholesky factorization of \mathbf{K}_N to approximate it by a lower rank matrix and solve the resulting eigenvalue problem with reduced cost [31, 46].

As an alternative we also tried using the random Fourier features (RFF) method to approximate \mathbf{K}_N by a lower rank matrix [47]. However, we found that a relatively large number of Fourier features was required to obtain a satisfactory approximation of \mathbf{K}_N , compared to the rank parameter r required for the partial Cholesky factorization [48]. The poor approximations obtained using the RFF method led to issues in the downstream bistochastic normalization of the approximate kernel matrix, which is why we did not use this approach in the present work.

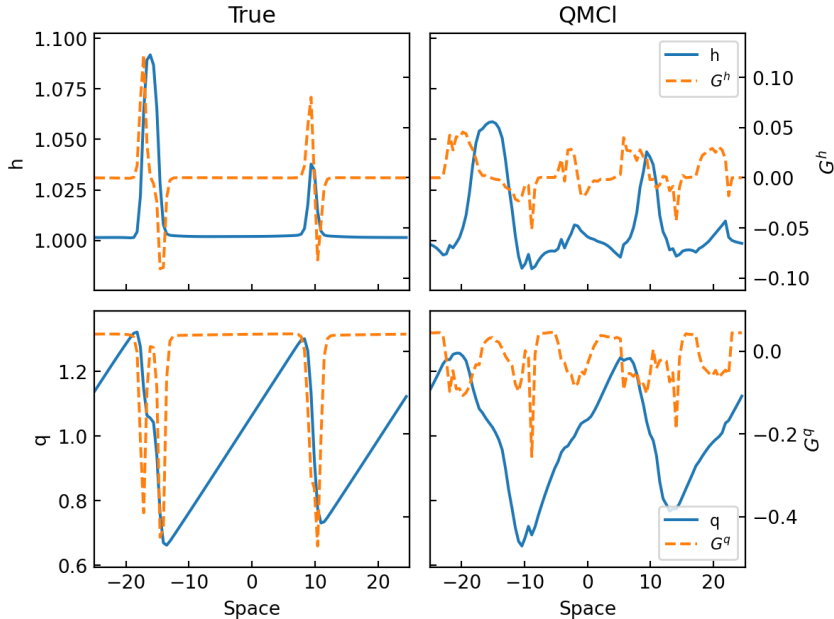


Figure 5: Spatial profiles of the final solution snapshot for the trajectory with $\delta = 0.75$. The layout of the plots is as in Figure 4.

In the online stage, the most expensive operation is the bayesian conditioning of the quantum density operators; more specifically, building the quantum effect operator from the current resolved state. To form the quantum effect operators we use kernel (13) to compare the current resolved product state vector to all product state vectors present in our training dataset. This is the only online operation that scales with the size of the training dataset NM , and requires that we have the training data loaded in memory throughout the online stage.

One way of alleviating this cost is to form a reduced representation of the training dataset and use it to build the quantum effect operators. For instance, one can employ the sampling algorithm underlying the partial Cholesky factorization algorithms [46] to extract a representative subset of the original training dataset, and rely only on that subset for the conditioning of the density operators. An alternative would be to use the RFF method to approximate the out of sample evaluation of kernel (13), thereby eliminating the dependence on the training data [47, 49]. In our case, this would require keeping in memory one $L \times L$ matrix for each random Fourier feature used, leading to an unsustainable memory cost.

In QMCI the surrogate fluxes are computed as the expected value of an observable with respect to a density operator. As a result, to compute fluxes that vary strongly over the spatial domain one has to ensure that the used density operators are very *sharp*: obtaining a clear maximum in some regions of product space Ω and being close to zero elsewhere, formally similar to a sum of Dirac delta measures. Working with such sharp density operators poses a number of computational challenges.

Producing accurate but very sharp density operators requires a very precise choice of the bandwidth parameter ϵ' used in kernel (13) for the bayesian conditioning. Having such a selective kernel means that the resulting density operators lead to highly accurate fluxes when the correct part of the training dataset is identified as dynamically relevant. However, it can lead to inaccurate fluxes when regions of the training dataset are misidentified as relevant, compared to using a less selective kernel that leads to wider averaging of the employed observable. Moreover, working with a very selective kernel makes it more likely that no part of the training dataset is identified as dynamically relevant, leading to an approximately zero feature vector and posterior density operator. In such a case, attempting to normalize the posterior density operator to unit norm can yield unpredictable results. Working with a wider, less selective kernel makes this

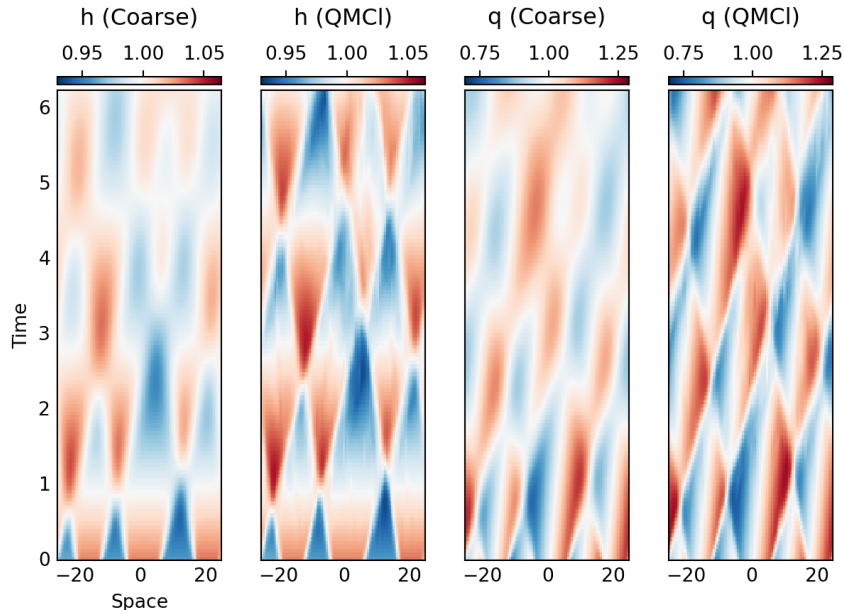


Figure 6: Space-time heatmaps for the trajectory with $\delta = 0.25$ comparing the dynamics on the coarse grid with the surrogate dynamics obtained by QMCI. From left to right, the first two plots show the results for the height field h , with the coarse grid results on the left and the QMCI results on the right; the next two plots show the results for the momentum field q , with coarse grid results on the left and QMCI on the right. The colorbars for each subplot are as in Figure 2.

scenario less likely to occur, albeit with the tradeoff of less informative conditioning and thus less accurate predicted fluxes. Finally, even if very sharp density operators can be consistently obtained, their accurate representation with respect to our eigenfunction basis will likely require a large number of eigenfunctions, leading to more expensive simulations.

The challenges involved in producing and working with very selective kernel functions motivate our use of a kernel bandwidth tuning algorithm [34] and of the introduction of variable bandwidth [37, 38]. These measures help us define a kernel function that is tailored to the characteristics of our training dataset, which in turn allows us to strike a reasonable compromise between numerical stability and sharpness of the kernel used for bayesian conditioning. As a result, we are able to construct a closure scheme that can predict the main features of the considered dynamics with reasonable computational cost and without numerical instabilities.

Theoretical aspects

One of the distinguishing features of the QMCI framework is that the classical dynamics is first embedded into the noncommutative setting of operator algebras used in quantum mechanics, and only then discretized to finite dimension. Namely, instead of directly discretizing functions on Hilbert space H to obtain functions on finite dimensional subspace H^L , we first map functions on H to operators in $B(H)$ and then discretize them to operators in $B(H^L)$. This process renders the discretization employed by QMCI positivity preserving, with positive classical observables and probability density functions mapped to positive definite operators.

In addition to positivity preservation, this discretization process embeds the discretized quantities in a space of larger dimension than direct discretization. More specifically, direct discretization maps real functions on H to functions on the L -dimensional subspace H^L . The QMCI discretization maps real functions on H to selfadjoint real operators in $B(H^L)$, which is a subspace of dimension $\frac{1}{2}L(L+1)$. A potential line of future research is exploring whether this difference in dimension, along with the noncommutative nature

of $B(H^L)$, allow QMCI to encode more statistical information about the original dynamics compared to closure schemes performed directly in H^L .

Another line of research concerns the out of sample performance of QMCI. In Sections 2.6 and 3.3 we considered training data generated from a finite collection of initial conditions, without making reference to an explicit process of generating these initial conditions. A natural next step is to consider an invariant measure μ that admits a decomposition into conditional measures μ_i , sampled from a probability distribution of initial conditions. Interesting questions in this direction are to characterize the behavior of our closure scheme as the number of sampled trajectories increases, and to derive associated out of sample error bounds.

4. Conclusion

We developed a framework for the dynamical closure of spatiotemporal dynamics which combines elements of the quantum mechanical closure (QMCI) framework developed in [13] and the vector valued spectral analysis (VSA) methodology of [14]. The presented framework encodes statistical information about the unresolved degrees of freedom of the considered dynamics in the form of a field of quantum density operators on the spatial domain. This results in a flexible architecture where density operators are collocated with the discretization cells of the coarse model for the resolved dynamics. The density operators communicate with the resolved dynamics by: (1) providing the required flux terms through the expected value of quantum observables; (2) receiving information through kernel feature maps. Importantly, our approach inherits the symmetry factorization properties of VSA during the basis construction process, and can also be used with training data consisting of multiple dynamical trajectories. As with the original QMCI work, the process of embedding the original dynamics into the noncommutative setting of quantum mechanics leads to the positivity preserving discretization of classical observables and probability density functions.

We applied QMCI to a closure problem for the shallow water equations on a periodic one dimensional domain. The numerical results demonstrate that QMCI can effectively predict the dynamics of the out of sample initial conditions tested in this work, generating height and momentum fields that agree both qualitatively and quantitatively with the true dynamics. As expected from the strong spatial variation of the subgrid fluxes, the QMCI surrogate dynamics is more diffusive than the true dynamics, and eventually struggles to fully capture the sharp spatial features of the true solution. Nevertheless, we believe that the results act as a successful proof of concept for the extension of QMCI to spatiotemporal dynamics, especially given the modest amount of data used for its training. Everything else kept the same, we expect that increasing the number of training samples or the spectral resolution will lead to improved prediction accuracy.

Future research directions include improving the computational cost of QMCI and the development of strategies for sampling initial conditions in the training stage. In addition, we plan to explore applications of QMCI to systems exhibiting chaotic spatiotemporal dynamics.

Acknowledgements

DG and JS acknowledge support from the U.S. Department of Energy under grant DE-SC0025101. CV was supported as a postdoctoral researcher from this grant. DG acknowledges support from the U.S. Department of Defense, Basic Research Office under Vannevar Bush Faculty Fellowship grant N00014-21-1-2946. DCF was supported as a PhD student from this grant. We thank Ilon Joseph, Michael Montgomery and Ilya Timofeyev for helpful conversations on the topics of this work.

Appendix A. Numerical implementation

The process of building and using the developed QMCI scheme to simulate the surrogate dynamics consists of two stages: the offline and online stages. Below we outline the steps followed in each stage.

Offline stage

The offline stage consists of the operations needed to build the QMCI scheme using the training samples for the resolved state variables $\{\hat{u}_n\}_{n=0}^{N-1}$ and the subgrid fluxes $\{f(u_n, \cdot)\}_{n=0}^{N-1}$. This involves the following sequence of steps.

1. Use the state samples $\{\hat{u}_n\}$ to calibrate the bandwidth parameter ϵ for the kernel (9) and perform its bistochastic normalization.
2. Use the state samples $\{\hat{u}_n\}$ to compute the leading L eigenfunctions $\{\phi_\ell\}$ of the normalized integral operator (12), defining the subspace H_N^L as their linear span. The eigenfunction basis is represented by the $NM \times L$ matrix Φ holding one eigenfunction in each column.
3. Form the transfer operator P_N^L and its $L \times L$ coefficients matrix \mathbf{P}_N^L .
4. Use the flux samples $\{f(u_n, \cdot)\}$ to form the two quantum observables $A_0, A_1 \in B(H_N^L)$, computing their $L \times L$ coefficients matrices \mathbf{A}_0 and \mathbf{A}_1 . Observable A_0 is built using the flux samples $\{f_0(x_n, \cdot)\}$ corresponding to the height h variables; observable A_1 using $\{f_1(x_n, \cdot)\}$ corresponding to the q variables.
5. Define the field of quantum density operators $\rho: S \rightarrow B(H_N^L)$, assigning one density operator to each coarse grid cell. For each gridpoint $x_m \in S_M$, the associated density operator $\rho(x_m)$ is represented by the vector $\boldsymbol{\rho}_m$ in \mathbb{R}^L .
6. Use the state samples $\{\hat{u}_n\}$ to calibrate the bandwidth parameter ϵ' of the kernel (13) and compute the bandwidth function needed for its variable bandwidth generalization.

Online stage

In the online stage we use the model built in the offline stage to timestep the surrogate dynamics. We denote by $\tilde{u} \in X_r$ the resolved state predicted by QMCI, to distinguish it from the true resolved state \hat{u} . The online stage consists of the following steps.

1. Initialize the resolved state \tilde{u} .
2. Initialize the density operators ρ representing each coarse grid cell by using an uninformative initial condition: set each density operator $\rho(x_m)$ to the projection along the unit function $1_N \in H_N^L$ that takes the value 1 everywhere.
3. Condition each density operator using the initial resolved state \tilde{u} and the training data $\{\hat{u}_n\}$.
4. Use the density operators ρ and the observables A_0 and A_1 to compute the surrogate fluxes \tilde{f} , corresponding to two flux values for each coarse grid cell.
5. Begin the timestepping loop.
 - (a) Update the resolved state \tilde{u} using the surrogate fluxes.
 - (b) Update the density operators ρ using the transfer operator.
 - (c) Condition the density operators ρ using the updated resolved state \tilde{u} and the state training samples $\{\hat{u}_n\}$.
 - (d) Compute the updated surrogate fluxes \tilde{f} .

In the timestepping loop as presented above, the bayesian conditioning of the density operators is performed every timestep. In our presented numerical results, we have instead elected to condition the density operators every 10 timesteps (Section 3.3).

References

- [1] P. Sagaut, Large eddy simulation for incompressible flows, Springer, Berlin, 2006.
- [2] W. E, Principles of multiscale modeling, Cambridge University Press, New York, 2011.
- [3] D. J. Stensrud, Parameterization schemes, Cambridge University Press, New York, 2013.

- [4] A. Arakawa, W. H. Schubert, Interaction of a cumulus cloud ensemble with the large-scale environment, Part I, *J. Atmos. Sci.* 31 (3) (1974) 674–701. doi:10.1175/1520-0469(1974)031<0674:IOACCE>2.0.CO;2.
- [5] P. R. Gent, J. C. McWilliams, Isopycnal mixing in ocean circulation models, *J. Phys. Oceanogr.* 20 (1) (1990) 150–155. doi:10.1175/1520-0485(1990)020<0150:IMIOCM>2.0.CO;2.
- [6] W. E. E. Engquist, X. Li, W. Ren, E. Vanden-Eijnden, Heterogeneous multiscale methods: a review, *Commun. Comput. Phys.* 2 (2007) 367–450.
- [7] W. W. Grabowski, P. K. Smolarkiewicz, CRCP: A cloud resolving convection parameterization of the tropical atmosphere, *Phys. D* 133 (1–4) (1999) 171–178.
- [8] I. Grooms, A. J. Majda, Efficient stochastic superparameterization for geophysical turbulence, *Proc. Natl. Acad. Sci.* 110 (12) (2013) 4464–4469.
- [9] G. W. Hammett, F. W. Perkins, Fluid moment models for Landau damping with application to the ion-temperature-gradient instability, *Phys. Rev. Lett.* 64 (1990) 3019–3022.
- [10] I. Joseph, A. M. Dimits, Connecting collisionless Landau fluid closures to collisional plasma physics models, *Contrib. Plasma Physics* 56 (6–8) (2016) 504–510.
- [11] C. Ma, B. Zhu, X.-Q. Xu, W. Wang, Machine learning surrogate models for Landau fluid closure, *Phys. Plasmas* 27 (4) (2020) 042502.
- [12] B. Laperre, J. Amaya, S. Jamal, G. Lapenta, Identification of high order closure terms from fully kinetic simulations using machine learning, *Phys. Plasmas* 29 (3) (2022) 032706.
- [13] D. C. Freeman, D. Giannakis, J. Slawinska, Quantum mechanics for closure of dynamical systems, *Multiscale Model. Simul.* 22 (1) (2024) 283–333. doi:10.1137/22M1514246.
- [14] D. Giannakis, A. Ourmazd, J. Slawinska, Z. Zhao, Spatiotemporal pattern extraction by spectral analysis of vector-valued observables, *J. Nonlinear Sci.* 29 (5) (2019) 2385–2445. doi:10.1007/s00332-019-09548-1.
- [15] C. Bardos, F. Golse, D. Levermore, Fluid dynamic limits of kinetic equations I: formal derivations, *J. Stat. Phys.* 63 (1–2) (1991) 323–344. doi:10.1007/BF01026608.
- [16] S. Rasp, M. S. Pritchard, P. Gentine, Deep learning to represent subgrid processes in climate models, *Proc. Natl. Acad. Sci.* 115 (39) (2018) 9684–9689.
- [17] J. Yuval, P. A. O’Gormann, Stable machine-learning parameterization of subgrid processes for climate modeling at a range of resolutions, *Nat. Commun.* 11 (2020) 3295.
- [18] H. J. Bae, P. Koumoutsakos, Scientific multi-agent reinforcement learning for wall-models of turbulent flows, *Nat. Commun.* 13 (2022) 1443.
- [19] A. Bracco, J. Brajard, H. A. Dijkstra, P. Hassanzadeh, C. Lessig, C. Monteleoni, Machine learning for the physics of climate, *Nat. Rev. Phys.* 7 (2025) 6–20.
- [20] T. N. Palmer, A nonlinear dynamical perspective on model error: a proposal for non-local stochastic-dynamic parametrization in weather and climate prediction models, *Quart. J. Roy. Meteorol. Soc.* 127 (2001) 279–304.
- [21] A. J. Majda, I. Timofeyev, E. Vanden Eijnden, Models for stochastic climate prediction, *Proc. Natl. Acad. Sci.* 96 (1999) 14687–14691.

- [22] A. J. Chorin, F. Lu, Discrete approach to stochastic parametrization and dimension reduction in nonlinear dynamics, *Proc. Natl. Acad. Sci. USA* 112 (2015) 9804–9809.
- [23] J. Berner, U. Achatz, L. Batté, L. Bengtsson, A. D. L. Cámara, H. M. Christensen, M. Colangeli, D. R. B. Coleman, D. Crommelin, S. I. Dolaptchiev, C. L. E. Franzke, P. Friederichs, P. Imkeller, H. Järvinen, S. Juricke, V. Kitsios, F. Lott, V. Lucarini, S. Mahajan, T. N. Palmer, C. Penland, M. Sakradzija, J.-S. Von Storch, A. Weisheimer, M. Weniger, P. D. Williams, J.-I. Yano, Stochastic parameterization: toward a new view of weather and climate models, *Bull. Amer. Meteor. Soc.* 98 (3) (2017) 565–588.
- [24] A. Lasota, M. C. Mackey, *Chaos, fractals, and noise*, 2nd Edition, Springer, New York, 1994. doi:10.1007/978-1-4612-4286-4.
- [25] B. C. Hall, *Quantum theory for mathematicians*, Springer, New York, 2013.
- [26] J. J. Sakurai, J. Napolitano, *Modern quantum mechanics*, 3rd Edition, Cambridge University Press, Cambridge, 2021.
- [27] D. Mauro, On Koopman–von Neumann waves, *Int. J. Mod. Phys. A* 17 (09) (2002) 1301–1325. doi:10.1142/S0217751X02009680.
- [28] D. I. Bondar, F. Gay-Balmaz, C. Tronci, Koopman wavefunctions and classical–quantum correlation dynamics, *Proc. R. Soc. A* 475 (2229) (2019) 20180879. doi:10.1098/rspa.2018.0879.
- [29] I. Joseph, Koopman–von Neumann approach to quantum simulation of nonlinear classical dynamics, *Phys. Rev. Res.* 2 (4) (2020) 043102. doi:10.1103/PhysRevResearch.2.043102.
- [30] P. Busch, P. J. Lahti, P. Mittelstaedt, *The quantum theory of measurement*, Springer, Berlin, 1996.
- [31] C. Vales, D. Giannakis, Accelerated decomposition of bistochastic kernel matrices by low rank approximation, arXiv:2510.26574 (2025). doi:10.48550/arXiv.2510.26574.
- [32] R. Temam, *Infinite-dimensional dynamical systems in mechanics and physics*, 2nd Edition, Springer, New York, 1997.
- [33] J. C. Robinson, *Infinite-dimensional dynamical systems*, Cambridge University Press, Cambridge, 2001.
- [34] R. R. Coifman, Y. Shkolnisky, F. J. Sigworth, A. Singer, Graph laplacian tomography from unknown random projections, *IEEE Trans. Image Process.* 17 (10) (2008) 1891–1899.
- [35] R. R. Coifman, M. J. Hirn, Bi-stochastic kernels via asymmetric affinity functions, *Appl. Comput. Harmon. Anal.* 35 (1) (2013) 177–180.
- [36] S. Das, D. Giannakis, J. Slawinska, Reproducing kernel Hilbert space compactification of unitary evolution groups, *Appl. Comput. Harmon. Anal.* 54 (2021) 75–136.
- [37] T. Berry, J. Harlim, Variable bandwidth diffusion kernels, *Appl. Comput. Harmon. Anal.* 40 (1) (2016) 68–96. doi:10.1016/j.acha.2015.01.001.
- [38] D. Giannakis, Data-driven spectral decomposition and forecasting of ergodic dynamical systems, *Appl. Comput. Harmon. Anal.* 47 (2) (2019) 338–396. doi:10.1016/j.acha.2017.09.001.
- [39] L.-S. Young, What are SRB measures, and which dynamical systems have them?, *J. Stat. Phys.* 108 (5/6) (2002) 733–754.
- [40] M. Blank, Ergodic averaging with and without invariant measures, *Nonlinearity* 30 (12) (2017) 4649–4664.

- [41] G. K. Vallis, Atmospheric and oceanic fluid dynamics, 2nd Edition, Cambridge University Press, Cambridge, 2017.
- [42] G. B. Whitham, Linear and nonlinear waves, Wiley, New York, 1999.
- [43] M. Zacharuk, S. I. Dolaptchiev, U. Achatz, I. Timofeyev, Stochastic subgrid-scale parametrization for one-dimensional shallow-water dynamics using stochastic mode reduction, *Q. J. R. Meteorol. Soc.* 144 (715) (2018) 1975–1990. doi:10.1002/qj.3396.
- [44] I. Timofeyev, A. Schwarzmann, D. Kuzmin, Application of machine learning and convex limiting to subgrid flux modeling in the shallow-water equations, *Math. Comput. Simul.* 238 (2025) 163–178. doi:10.1016/j.matcom.2025.04.031.
- [45] R. J. LeVeque, Finite volume methods for hyperbolic problems, Cambridge University Press, New York, 2002.
- [46] Y. Chen, E. N. Epperly, J. A. Tropp, R. J. Webber, Randomly pivoted Cholesky: practical approximation of a kernel matrix with few entry evaluations, *Comm. Pure Appl. Math.* 78 (2024) 995–1041. doi:10.1002/cpa.22234.
- [47] A. Rahimi, B. Recht, Random features for large-scale kernel machines, in: *Advances in Neural Information Processing Systems*, Vol. 20, Curran Associates, 2007, pp. 1177–1184.
- [48] T. Yang, Y.-F. Li, M. Mahdavi, R. Jin, Z.-H. Zhou, Nyström method vs random Fourier features: a theoretical and empirical comparison, in: *Advances in Neural Information Processing Systems*, Vol. 25, Curran Associates, 2012, pp. 476–484.
- [49] D. Giannakis, A. Henriksen, J. A. Tropp, R. Ward, Learning to forecast dynamical systems from streaming data, *SIAM J. Appl. Dyn. Syst.* 22 (2) (2023) 527–558. doi:10.1137/21M144983X.